JOURNAL OF PROPULSION AND POWER
Vol. 22, No. 6, November–December 2006

Propulsive Performance of Airbreathing Pulse Detonation Engines

Fuhua Ma,* Jeong-Yeol Choi,† and Vigor Yang‡
Pennsylvania State University, University Park, Pennsylvania 16802

DOI: 10.2514/1.21755

The propulsive performance of airbreathing pulse detonation engines at selected flight conditions is evaluated by means of a combined analytical/numerical analysis. The work treats the conservation equations in axisymmetric coordinates and takes into account finite-rate chemistry and variable thermophysical properties for a stoichiometric hydrogen/air mixture. In addition, an analytical model accounting for the state changes of the working fluid in pulse detonation engine operation is established to predict the engine performance in an idealized situation. The system under consideration includes a supersonic inlet, an air manifold, a valve, a detonation tube, and a convergent–divergent nozzle. Both internal and external modes of valve operation are implemented. Detailed flow evolution is explored, and various performance loss mechanisms are identified and quantified. The influences of all known effects (such as valve operation timing, filling fraction of reactants, nozzle configuration, and flight condition) on the engine propulsive performance are investigated systematically. A performance map is established over the flight Mach number of 1.2–3.5. Results indicate that the pulse detonation engine outperforms ramjet engines for all the flight conditions considered herein. The benefits of pulse detonation engines are significant at low-supersonic conditions, but gradually decrease with increasing flight Mach number.

Nomenclature

A	=	preexponential factor
A_e	=	area of engine exit plane
c	=	speed of sound
c_p	=	constant-pressure specific heat
e_t	=	specific total energy
F	=	instantaneous thrust
F_{sp}	=	specific thrust

Fuhua Ma is a Postdoctoral Research Associate of Mechanical Engineering at the Pennsylvania State University, receiving his B.S. and M.S. degrees from the University of Science and Technology of China and his Ph.D. from the Pennsylvania State University. His research interests include computational fluid dynamics, parallel computing and system, shock- and detonation-wave dynamics, chemically reacting flow, high-speed flow, and modeling and performance analysis of various propulsion systems such as ramjets, scramjets, and pulse detonation engines. He is the author or coauthor of more than 40 technical papers and book chapters in his research fields. He was the recipient of the 2004 AIAA best paper award in airbreathing propulsion. He has been serving as an active reviewer for several journals and also serves as a system manager for a large in-house Linux cluster at Pennsylvania State University. He is a member of AIAA and the Combustion Institute.

Jeong-Yeol Choi is an Associate Professor of Aerospace Engineering at the Pusan National University, Korea, receiving his B.S., M.S., and Ph.D. degrees from the Seoul National University, Korea. He has been a visiting assistant professor at Pennsylvania State University. Currently, he is the department chair and BK21 program head of his department at Pusan National University. His research topics are focused on high-fidelity CFD modeling of supersonic reactive flows including supersonic combustion, detonation, and plasma flows in aerospace propulsion systems from gas turbine, ramjet and scramjet engines, liquid rocket engine, and arcjet thruster. Also, he has given large attention to the novel propulsion concepts, such as ram accelerators, laser propulsion, and detonation applications in propulsion. He is the author or coauthor of more than 40 international and domestic archival papers. He was the recipient of publication and technical awards from AIAA, the Combustion Institute, KSPE (Korean Society of Propulsion Engineers), and Samsung Electronics, Inc. He is a senior member of AIAA and several other academic societies. He serves on the editorial boards of the KSPE journal and the KSAS (Korean Society of Aerospace Sciences) journal.

Vigor Yang is a Distinguished Professor of Mechanical Engineering at the Pennsylvania State University, receiving his B.S. from the National Tsing Hua University and his Ph.D. from the California Institute of Technology. His research interests include combustion instabilities in propulsion systems, chemically reacting flows in air-breathing and rocket engines, combustion of energetic materials, and high-pressure thermodynamics and transport. He has supervised 41 Ph.D. and 15 M.S. theses. He is the author or coauthor of more than 250 technical papers in the areas of propulsion and combustion and has published nine comprehensive volumes on rocket and air-breathing propulsion. He was the recipient of the Penn State Engineering Society Premier Research Award and several publication and technical awards from AIAA. Dr. Yang serves on the editorial advisory boards of *Combustion and Flame*, *Progress in Energy and Combustion Science*, *Combustion, Explosion, and Shock Waves*, *Journal of the Chinese Institute of Engineers*, and the newly established *JANNAF Journal of Propulsion and Energetics*. He has been a consultant to many U.S. rocket and gas-turbine engine companies as well as government organizations. Dr. Yang is a Fellow of the AIAA and American Society of Mechanical Engineers.

Received 12 December 2005; revision received 22 June 2006; accepted for publication 22 June 2006.

*Postdoctoral Research Associate, Department of Mechanical Engineering; mafuhua@psu.edu. Member AIAA.
†Visiting Associate Professor, Department of Mechanical Engineering; juc16@psu.edu.
‡Distinguished Professor, Department of Mechanical Engineering; vigor@psu.edu. Fellow AIAA.

f = fuel-to-air mass ratio of reactants
$\tilde{f}$ = overall fuel-to-air mass ratio of the mixture of reactants and purge air
g = gravitational acceleration
I_{sp} = specific impulse
I = impulse
L = length of detonation tube
L_{driv} = length of driver gas in detonation tube
L_f = length of filled reactant at the end of filling stage
L_p = length of purge air at the end of purging stage
M_1 = Mach number of filling gas
M_∞ = Mach number of freestream
$\dot{m}_a$ = mass flow rate of air delivered to engine
$\dot{m}_e$ = mass flow rate at engine exit plane
$\dot{m}_f$ = mass flow rate of fuel delivered to engine
$\boldsymbol{n}$ = unit vector normal to surface
n_x = axial component of unit vector normal to surface
p_e = area-averaged pressure at engine exit plane
p_r = reservoir pressure for purging and filling
p_{t1} = total pressure at combustor entrance
p_v = threshold pressure for valve open
q = heat release per unit mass of reactants
$\tilde{q}$ = overall heat release per unit mass of mixture of reactants and purge air
R = gas constant
R_u = universal gas constant
r_{th} = nozzle throat radius
r_{tube} = detonation-tube radius
s = specific entropy
T_a = activation temperature
T_{t1} = total temperature at combustor entrance
u = axial velocity
$\boldsymbol{u}$ = velocity vector
u_e = mass-averaged axial velocity at engine exit plane
v = vertical velocity
W = molecular weight
Z = mass fraction
β = ratio of purge to valve-open time, τ_{purge}/τ_{open}
β_f = filling fraction, L_f/L
β_p = purge fraction, L_p/L
γ = ratio of specific heat
η_{th} = thermodynamic cycle efficiency
ρ = density
τ = time period
τ_{close} = valve-closed period during which valve is closed
τ_{cycle} = cycle period
τ_{fill} = filling period
τ_{open} = valve-open period during which valve is open
τ_{purge} = purging period
ϕ = equivalence ratio
$\dot{\omega}$ = mass production rate

Subscripts

D = detonation wave
e = engine exit plane
i = species index
1 = nominal species 1 (reactant)
2 = nominal species 2 (product), or Chapman–Jouguet state
3 = nominal species 3 (air)
∞ = freestream

Superscript

$(\bar{\ })$ = time- or cycle-averaged properties

I. Introduction

PULSE detonation engines (PDEs) are unsteady propulsion devices that produce thrust by using repetitive propagating detonation. Extensive efforts have been applied to circumvent several challenging engineering problems associated with the development of PDEs. These include fuel injection and mixing, repetitive detonation initiation, integration of detonation tubes with inlet and nozzle, and overall system optimization [1,2]. In spite of the progress made to date, there still remains a major concern about the propulsive performance of PDEs, especially in comparison with such well-established propulsion systems as ramjet and gas-turbine engines. The issue has been addressed by many researchers by means of experimental, theoretical, and numerical methods. Significant discrepancies, however, exist among these results, partly due to different system configurations and operating conditions considered in each study. Another factor contributing to this phenomenon is uncertainties inherent in various modeling and measurement techniques. The lack of a well-defined paradigm for the system configuration that allows the benchmark of model predictions against experimental data poses another challenge. The purpose of this paper is to establish a combined theoretical/numerical framework to faithfully predict the propulsive performance of a model PDE. Various fundamental processes and design attributes, as well as operating parameters, will be examined systematically in terms of their effects on the PDE performance.

This paper is organized as follows. Section II defines and reviews the propulsive performance parameters. Section III describes the model PDE considered as well as its operation and underlying assumptions. Sections IV and V outline the numerical and analytical framework, respectively. In Sec. VI, the thrust chamber dynamics and propulsive performance of the model PDE are investigated over a broad parameter space that includes operation timing, threshold pressure for valve open, filling fraction of reactants, nozzle configuration, and flight condition. A comparison with the ramjet performance is also discussed.

II. Propulsive Performance Parameters

Following common practice, the propulsive performance of a PDE can be characterized by the specific impulse, defined as the thrust per unit weight flow rate of fuel or the impulse per unit weight of fuel:

$$I_{sp} \equiv \frac{\bar{F}}{\bar{\dot{m}}_f g} \equiv \frac{I}{m_f g} \tag{1}$$

A similar parameter is the specific thrust, defined as the thrust per unit mass flow rate of air or the impulse per unit mass of air:

$$F_{sp} \equiv \frac{\bar{F}}{\bar{\dot{m}}_a} \equiv \frac{I}{m_a} \tag{2}$$

The mass flow rates of air and fuel delivered to the engine are denoted by $\dot{m}_a$ and $\dot{m}_f$, respectively. Overbars are used in the above expressions to represent cycle-averaged or time-averaged quantities accounting for the intrinsic unsteadiness of PDE operation.

Several different definitions of thrust are adopted in existing studies on PDEs. The first is the standard engine-net thrust, which can be derived by applying the momentum conservation over a control volume enclosing the engine of concern [3,4],

$$F = \dot{m}_e u_e - \dot{m}_a u_\infty + (p_e - p_\infty)A_e + \int_{CV} \frac{\partial \rho u}{\partial t}\, \mathrm{d}V \tag{3}$$

where the mass flow rate $\dot{m}_e$, velocity u_e, and pressure p_e at the engine exit (S_e) are spatially averaged over the transverse plane.

$$\dot{m}_e = \int_{S_e} \rho \boldsymbol{u} \cdot \boldsymbol{n}\, \mathrm{d}S \tag{4}$$

$$u_e = \frac{1}{\dot{m}_e} \int_{S_e} \rho u \boldsymbol{u} \cdot \boldsymbol{n}\, \mathrm{d}S \tag{5}$$

$$p_e = \frac{1}{A_e} \int_{S_e} p\, \mathrm{d}S \tag{6}$$

The time-averaged momentum balance takes the form

$$\bar{F} = \overline{\dot{m}_e u_e} - \dot{m}_a u_\infty + (\bar{p}_e - p_\infty)A_e \tag{7}$$

The second definition, referred to as engine-gross thrust, does not include the momentum of the incoming air:

$$\bar{F}^g = \overline{\dot{m}_e u_e} + (\bar{p}_e - p_\infty)A_e \tag{8}$$

The third definition, referred to as chamber-wall thrust, is based on the pressure force acting on the inner wall of the thrust chamber (including the detonation tube and exhaust nozzle):

$$\bar{F}^c = \int_{S_{cw}} (\bar{p} - p_\infty) n_x \, \mathrm{d}S \tag{9}$$

For cases involving only simple detonation tubes, the chamber-wall thrust reduces to the pressure force on the closed end of the tube and is normally known as the detonation-tube thrust in the literature [1,5]. This term has been commonly used in most single-pulse studies [5–12], whereas the gross and net thrusts are usually applied for limit-cycle operations [3,4,13–18].

The relationship between the chamber-wall and engine-gross thrusts can be best understood by considering the following momentum balance for a limit-cycle operation:

$$\begin{aligned}\bar{F}^c &= [\overline{\dot{m}_e u_e} + (\bar{p}_e - p_\infty)A_e] - [\overline{\dot{m}_i u_i} + (\bar{p}_i - p_\infty)n_{ix}A_i] \\ &= \bar{F}^g - [\overline{\dot{m}_i u_i} + (\bar{p}_i - p_\infty)n_{ix}A_i]\end{aligned} \tag{10}$$

where the subscript i stands for the air/fuel injection surface, and n_{ix} the axial component of the unit vector normal to the surface. This equation indicates that the chamber-wall thrust is less or equal to the engine-gross thrust, because the second term on the right-hand side is generally positive. In some situations, the air and fuel are injected from the lateral surface of a detonation tube such that $u_i = 0$ and $n_{ix} = 0$. The chamber-wall thrust becomes identical to engine-gross thrust.

In numerical simulations, the above three commonly used thrusts can be directly calculated based on their respective definitions. In experiments, thrust is usually measured using such equipment as a ballistic pendulum, a load cell, a damped thrust stand, and a spring-damper system. These techniques measure the actual force on a test rig, combining both thrust and drag. The pressure and viscous forces acting on the external surface of the system are often neglected in a laboratory direct-connect test. A single-pulse operation of a simple detonation tube does not take into account the effects of chamber filling, and most experimental data are acquired from the measurements of wall pressure. As for the limit-cycle operation of a test rig including filling and control modules, the measurements are limited to engine-gross thrust. To obtain the engine-net thrust, the equivalent flight condition should be deduced according to the filling conditions, such that the influence of the incoming inflow can be appropriately treated in conducting the momentum balance.

Both hydrogen and hydrocarbon fuels have been employed in the studies of PDEs. The latter include gaseous fuels such as ethylene (C_2H_4) and propane (C_3H_8) and liquid fuels such as JP10 ($C_{10}H_{16}$). Ethylene was selected by many researchers because of its well-documented detonation properties. It is also a major product from the thermal decomposition of many heavy hydrocarbon fuels for airbreathing propulsion applications. Hydrogen was broadly employed, especially in numerical studies, because of its relatively simple chemical kinetics and ease of detonation. To facilitate comparison with existing studies, the present work is limited to hydrogen-fueled airbreathing PDEs. Table 1 summarized the performance data obtained from various experimental, numerical, semi-empirical, and analytical studies of hydrogen/air systems [3–19]. Some analytical works, such as those of Heiser and Pratt [20] and Talley and Coy [21], are not listed in the table because they are so general that they can be easily applied to all the cases considered.

Several techniques have been commonly used to measure performance parameters. The most straightforward one lies in the integration of the pressure force at the closed end of a detonation tube. The method does not require a complex facility, but can only be implemented in a simple system. Another usually employed in single-pulse experiments is the ballistic-pendulum technique, in which the detonation tube is suspended as a pendulum by support wires, and the impulse is determined by measuring the maximum horizontal deflection of the tube [22]. In multicycle experiments, the load-cell technique is often implemented. The force history is directly measured by a load cell attached to the detonation tube through a cage [6]. Because negative thrust cannot be recorded, the impulse may be overestimated. In addition, the structural response needs to be taken into account. Other reported techniques include the damped thrust stand [14] and the spring-damper system [23]. In view of the limitation of each technique, a combination of them may be required to obtain a reliable impulse measurement. Hinkey et al. [6] measured the impulse in their single-pulse experiments by means of both the wall-pressure and load-cell techniques and found that the former is about 20% lower than the latter. In numerical studies, the performance can be directly determined based on the calculated flowfield. However, uncertainties associated with theoretical models and numerical solutions may significantly affect the accuracy of predicted results.

The propulsive performance of a PDE depends on its system configuration and operating conditions. In Table 1, the third column lists the length and internal diameter of the detonation tube as well as the length of the exhaust nozzle. Other details such as the enhancement of deflagration-to-detonation transition (DDT) (e.g., the Shchelkin spiral, blockage plate, and coannulus) often adopted in experiments are not included for brevity, in spite of its effect on performance. All of the numerical simulations did not consider DDT. Detonation is directly initiated by high-pressure, high-temperature gases. In reality, the initiation energy may play a substantial role in determining the system performance and should be carefully accessed.

Two different kinds of operations (i.e., single pulse and cyclic) have been conducted. The former refers to an operation that only consists of detonation initiation, wave propagation, and product-gas blowdown, whereas the latter contains the entire operation including the low-energy flow processes during the purging and filling stages, as well as losses associated with air delivery and fuel distribution. As a consequence, the performance of a single-pulse operation is generally higher than that of the cyclic operation. Two different valve-control modes have been implemented in cyclic operations, as detailed in Sec. III. In the external mode, the valve opens and closes at prespecified times, whereas in the internal mode, the valve operation is based on the flow conditions inside the detonation tube. Dual-mode operations are adopted in some studies.

To date, most experiments and numerical simulations were based on direct-connect tests. Only a few numerical studies have considered real flight conditions. Ma et al. [3,4] and Wu et al. [17] considered a design with a flight altitude of 9.3 km and a Mach number of 2.1. The same flight altitude was treated by Harris et al. [18] with the flight Mach numbers in the range of 1.2–3.5. The flow losses through the engine inlet were properly taken into account in these works.

Several observations are made of Table 1. First, the specific impulse of a straight detonation tube with a single-pulse operation is around 4300 s for a stoichiometric H_2-air mixture at 1 atm and 298 K. The much lower experimental value of Hinkey et al. [6] can be attributed to the inclusion of the predetonator mixture (H_2/O_2) as fuel in the calculation of specific impulse. The higher numerical value of Kailasanath et al. [8] results from the use of a large ignition source in their study.

Second, most experiments with cyclic operations were conducted in a frequency range much lower than that for numerical simulations, mainly due to hardware limitations and difficulties of initiating detonation. Such a disparity of frequency range has given rise to some controversial conclusions between experiments and simulations. For low-frequency operations, the pressure in the

Table 1 Propulsive performance of hydrogen-fueled airbreathing PDEs

Reference	Method	Configurations	Operation conditions	I_{sp}, s	Type/remarks
			Single-pulse operation of detonation tube		
Hinkey et al. [6] (1995)	Experimental load cell	$L = N/A$, $D = 5.1$ cm without nozzle	$\phi = 1.0$, 1 atm, 298 K H_2/O_2 as predet. mixture	1200 (load cell), 1000 (wall pres.)	Chamber; low due to use of predet. mixture
Wintenberger et al. [5] (2003)	Semi-empirical	$L = N/A$ without nozzle	$\phi = 1.0$, 1 atm, 300 K	4366	Chamber
Endo et al. [7] (2004)	Analytical	Straight tube	$\phi = 1.0$, 1 atm, 300 K	4215	Chamber
Kailasanath et al. [8] (1999)	Numerical, 1-D 8-sp. 48-re.	$L = 20$ cm without nozzle	$\phi = 1.0$, 1 atm, 298 K	4850–7930 (on exit BC)	Chamber
Radulescu and Hanson [9] (2005)	Numerical, 1-D $\gamma = 1.16$	$L = N/A$ without nozzle	$\phi = 1.0$, 1 atm, 298 K	4270	Chamber
Yungster [10] (2003)	Numerical, axisym. 9-sp. 19-re.	$L = 100$ cm, $D = 6.6$ cm without nozzle	$\phi = 1.0$, 1 atm, 298 K	4360	Chamber
Tangirala et al. [11] (2003)	Numerical, axisym. 7-sp. 23-re.	$L = 100$ cm, $D = 7.6$ cm without nozzle	$\phi = 1.0$, 1 atm, 298 K	4360	Chamber
Perkins and Sung [12] (2005)	Numerical, 2-D 7-sp. 7-re.	$L = 30$ cm, $H = 10$ cm without nozzle	$\phi = 1.0$, 1 atm, 300 K	4429	Chamber
			Limit-cycle operation of thrust chamber		
Fong and Nalim [19] (2000)	Numerical, 1-D single γ	$L = 10.2$ cm without nozzle	Sea level, $f = 30$–159 Hz, $\phi = 1.0$, $p_v = 1$ atm, $p_r = N/A$ valve closes by timing	4000–5000 (on frequency)	Chamber
Aarnio et al. [13] (1996)	Experimental load cell	$L = 121.9$ cm, $D = 5.1$ cm without nozzle	Sea level, $f = 5$ Hz, $\phi = 1.0$, timing unknown	1116 (load cell), 1333 (wall pres.)	Gross; low due to use of predet. mixture
Schauer et al. [14] (2001)	Experimental damped thrust stand	$L = 91.4$ cm, $D = 5.1$ cm without nozzle	Sea level, $f = 16$ Hz, $\phi = 1.0$, external timing	4200–7100 (on fill fraction)	Gross
Cambier and Adelman [15] (1988)	Numerical, 1-D 7-species	$L = 50$ cm, $D = 6$ cm diverg. nozzle of 43 cm	Sea level, $f = 667$ Hz, $\phi = 1.0$, $p_v = 3.5$ atm, $p_r = N/A$ valve closes by timing	6507	Gross
Cambier and Tegner [16] (1998)	Numerical, 1-D Mozart code	$L = 10$ cm, $D = 2$ cm diverg. nozzle of 5 cm	Sea level, $f = 2080$–2600 Hz, $\phi = 1.0$, $p_v = 2$ atm, $p_r = 5$ atm valve closes by fill fraction	3540–4100 (on fill fraction)	Gross
			Limit-cycle operation of engine		
Wu et al. [17] (2003)	Nnumerical, 1-D single γ	$L = 60$ cm CD nozzle of 20 cm	$h = 9.3$ km, $M_\infty = 2.1$, $\phi = 1.0$, $f = 200$–400 Hz, $p_r = 0.8 p_{t\infty}$, external timing	~3676 (on timing)	Net; single-γ model may underpredict performance
Ma et al. [3] (2005)	Numerical, 2-D single γ	$L = 60$ cm, $H = 16$ cm without nozzle	$h = 9.3$ km, $M_\infty = 2.1$, $\phi = 1.0$, $f = 333$ Hz, $p_r = 0.8 p_{t\infty}$, external timing	~2355 (on timing)	Net; single-γ model may underpredict performance;
		$L = 60$ cm, $H = 16$ cm CD nozzles of 20 cm	$h = 9.3$ km, $M_\infty = 2.1$, $\phi = 1.0$, $f = 250$–400 Hz, $p_r = 0.8 p_{t\infty}$, external timing	~3672 (on timing)	performance can be improved by further optimization of
Ma et al. [4] (2005)	Numerical, 2-D single γ	$L = 40$–60 cm, $H = 5$ cm CD nozzle of 20 cm, 3 tubes	$h = 9.3$ km, $M_\infty = 2.1$, $\phi = 1.0$, $f = 250$–333 Hz, $p_r = 0.8 p_{t\infty}$, external timing	~3870 (on timing)	nozzle configuration
Harris et al. [18] (2006)	Numerical, axisym. three-γ	$L = 60$ cm, $D = 4.8$ cm CD nozzle of 10.9 cm	$h = 9.3$ km, $M_\infty = 1.2$–3.5, $\phi = 1$, $f = 60$–126 Hz, $p_v = p_r = 0.8 p_{t\infty}$, valve closes by timing	4000 ($M_\infty = 1.2$), 4547 ($M_\infty = 2.1$), 4900 ($M_\infty = 3.0$), 4950 ($M_\infty = 3.5$)	Net
Present work	Numerical, axisym. three-γ	$L = 50$ cm, $D = 10$ cm CD nozzle of 15 cm	$h = 1.5$ km, $M_\infty = 1.2$, $\phi = 1.0$, $h = 9.3$ km, $M_\infty = 2.1$, $\phi = 1.0$, $h = 15.5$ km, $M_\infty = 3.5$, $\phi = 1.0$, $f = 160$–292 Hz, $p_v = 0.95 p_r$, external and internal timing	3820 ($M_\infty = 1.2$), 5020 ($M_\infty = 2.1$), 5070 ($M_\infty = 3.5$)	Net

detonation tube reaches its ambient value after a lengthy blowdown process. The tube pressure remains at the ambient condition during the filling process and no thrust is produced. Thus, the multicycle performance approaches its single-pulse counterpart. The situation, however, considerably changes in the high-frequency range. The blowdown process may become so short that it can easily interact with the filling process. The state of filled reactants and the resultant propulsive performance may differ significantly from those of the first pulse, as will be elaborated later.

Table 1 also indicates the improvement of predicted performance parameters from a single-γ to a variable-γ model. The former employs a single set of specific-heat ratio (γ) and gas constant for all the gases included in PDE operation, whereas the latter takes into consideration the variations for reactants, products, and air. Our previous work [3,4] is based on a single-γ model to investigate the thrust chamber dynamics of both single and multitube PDEs. Although the approach produces accurate detonation wave speed and Chapman–Jouguet (CJ) properties, the use of the same set of gas dynamic parameters for reactants and combustion products may underpredict the flow expansion efficiency in the blowdown stage. Gases with larger γ's produce less work during expansion and consequently lead to a lower system performance. The effect of variable γ was also studied by Harris et al. [18] and Tangirala et al [24].

III. System Configuration and Operation

Pulse detonation engines differ from conventional engines in two major ways: unsteady operation and detonative combustion. A typical cycle of airbreathing PDE operation includes four basic phases: initiation and propagation of detonation wave, blowdown of combustion products, filling of purge gas, and recharge of reactants. To prevent inlet unstart caused by detonation-induced high-pressure gases in the chamber, the engine generally requires an inlet/combustor interface to isolate the chamber flow from traveling into the inlet. Two different kinds of interface (i.e., valved and valveless) [2] have been realized. In the valved design, the interface is a mechanical valve located at the head end of the detonation tube. The valve is closed during detonation initiation and propagation, but remains open during the filling and purging stages. In the valveless design, the isolation between the inlet and the combustor is achieved through a gasdynamic means [25,26]. Such design is mechanically simpler and circumvents the disadvantage associated with airflow stagnation in the valved design. The inclusion of an isolator, however, may limit the operation frequency. More details on PDE designs can be obtained from Roy et al. [2]. The present paper will only focus on valved airbreathing PDEs.

A. Physical Model and Flight Condition

Figure 1 shows schematically the system under consideration. It includes a coaxial supersonic inlet, an air manifold, a valve, a combustion chamber consisting of single or multiple detonation tubes, and a common convergent–divergent (CD) nozzle [3,4]. The manifold provides a buffer zone between the inlet and combustor, in which fuel and air are mixed before entering the combustor. Four representative flight conditions are investigated, as summarized in Table 2. The baseline condition involves an altitude of 9.3 km and a Mach number of 2.1. The freestream static pressure and temperature are 0.29 atm and 228 K, respectively, and the corresponding total pressure and temperature are 2.65 atm and 428 K.

The inlet is designed to capture and supply a stable airflow at a rate demanded by the combustor and to maintain a high-pressure recovery and stability margin at various engine operating conditions [27]. The total pressure recovery of the inlet flow is determined in accordance with the following military standard [28]:

$$\eta_{\mathrm{mil}} = 1 - 0.075(M_\infty - 1)^{1.35} \tag{11}$$

The flow loss resulting from the valve operation and reactant distribution should also be considered. A rigorous assessment of such a loss requires substantial computational efforts that may not be justified in the present study. An empirical pressure loss of 5% is thus assumed for all the flight conditions considered herein. The total pressure (p_{t1}) and total temperature (T_{t1}) at the combustor entrance are also listed in Table 2.

As a specific example, only one detonation tube is considered measuring 50 cm in length and 10 cm in diameter. The latter is larger than the H_2-air detonation cell size at the flow conditions encountered herein, in order to permit successful propagation of detonation wave within the tube. Detonation initiation represents a major challenge in the PDE design. In general, direct initiation of

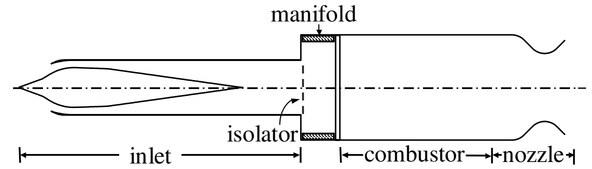

Fig. 1 Supersonic airbreathing pulse detonation engine.

detonation is impractical for repetitive operation due to limitations of energy supply and time response. Much effort has been applied to develop reliable and efficient initiation methods through either a DDT process or the use of a predetonator [14,22,25]. For engine performance predictions in the present work, detonation is directly initiated near the head end of the chamber by means of a small amount of driver gas.

The issue of nozzle optimization remains unresolved due to difficulties arising from the inherent flow unsteadiness in a nozzle and its strong interaction with other parts of an engine. Ideally, the nozzle configuration should adapt itself to the instantaneous local flow conditions. It is, however, formidable to design and fabricate such a flexible nozzle with adaptation on time scales commensurate with the PDE operation. Although not strictly proved, a CD nozzle appears to be more suited for PDEs than other configurations because of the advantages of preserving the chamber pressure during the blowdown and filling processes and providing more thrust surface area during the exhaust of detonation products [3,17,18,24]. The present paper thus focuses only on CD nozzles. Figure 2 shows the nozzle configurations considered herein. The length is 15 cm, of which 5 cm is the convergent section and 10 cm the divergent section. The radii at the nozzle entrance and exit are identical to that of the detonation tube. The nozzle contour contains two circular arcs, each with a radius equal to one-half of that of the detonation tube, and two straight sections with smooth connections. The nozzle configuration is determined by only one independent parameter: the nozzle throat radius r_{th}, to simplify the design optimization. Table 3 lists the geometric parameters of six different nozzle configurations, including the throat radius r_{th}, convergent angle θ_c, divergent angle θ_d, and area-expansion ratio r_e^2/r_{th}^2.

The computational domain shown in Fig. 3 includes the detonation tube and nozzle as well as an external region to remove uncertainties in specifying the boundary conditions at the nozzle exit. A large external region, as compared to the detonation tube, is selected to minimize wave reflections from the external boundaries. The entire domain is discretized into 111,446 unstructured triangular cells, of which 30,000 are located in the detonation tube, 7500 in the nozzle, and 73,946 in the external region. The grid size within the tube is about 1.7 mm in the axial direction, sufficient to resolve detonation propagation in the chamber. A grid-independence analysis was conducted to ensure numerical accuracy. The current grid is not intended to resolve detailed structures of a detonation wave front, which would require a much finer grid [29] not practical nor necessary for a system-level analysis of PDE performance.

B. Operation Sequence

The engine operation is controlled by the valve located at the entrance of the combustor. For simplicity, the valve is assumed to be either fully closed or fully open, with its open area identical to the

Table 2 Flight conditions and combustor entrance conditions

No.	M_∞	h, km	T_∞, K	p_∞, atm	$T_{t\infty}$, K	$p_{t\infty}$, atm	q, kPa	p_{t1}, atm	T_{t1}, K
1	1.2	1.5	278	0.83	358	2.02	85[a]	1.90	358
2	2.1	9.3	228	0.29	428	2.65	91	2.30	428
3	3.5	15.5	217	0.11	747	8.43	96	5.94	747
4	5.0	24.0	220	0.029	1323	15.5	52	7.55	1323

[a]Dynamic pressure q is calculated as $q = \gamma M_\infty^2 p_\infty/2$.

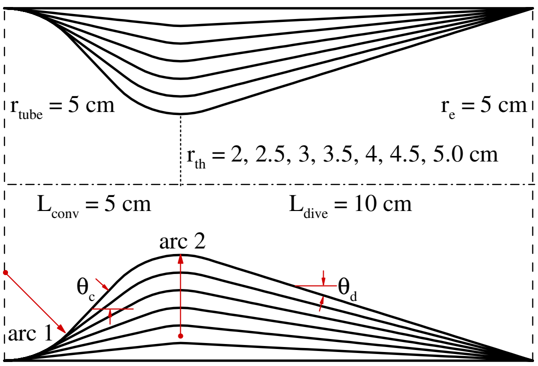

Fig. 2 Nozzle configurations.

cross-sectional area of the detonation tube. Both external and internal modes of valve operation [3,4,16,30] are considered in the present work. In the external mode, the engine operation sequence is described by three different time periods: the valve-closed period (τ_{close}) during which the valve is closed and the tube undergoes detonation initiation and propagation as well as blowdown of combustion products, the purging period (τ_{purge}) during which a small amount of cold air is injected into the tube to prevent preignition of fresh reactants, and the filling period (τ_{fill}) during which the combustible mixture is delivered to the tube. The above three segments constitutes a cycle period:

$$\tau_{\mathrm{cycle}} = \tau_{\mathrm{close}} + \tau_{\mathrm{open}} = \tau_{\mathrm{close}} + \tau_{\mathrm{purge}} + \tau_{\mathrm{fill}} \tag{12}$$

The internal mode of operation requires one pressure and two chemical sensors. The valve opens and the purging process begins when the pressure at the closed end of the tube falls below a prespecified threshold value (p_v). The air purge then terminates and the chamber filling begins when the purge gas reaches a prespecified axial location (L_p). Finally, the filling process completes and the valve closes when fresh reactants reach a prespecified axial location (L_f). The entire operation is controlled by three parameters: threshold pressure p_v, purge fraction β_p, and filling fractions β_f.

$$\beta_p = L_p/L, \qquad \beta_f = L_f/L \tag{13}$$

The internal-mode operation has been implemented by Cambier and Tegner [16] in their numerical simulations for a chamber consisting of a detonation tube and a divergent nozzle. The work, however, becomes much more complicated in the present study with CD nozzles. As a consequence of the complicated flow evolution in the chamber, it is not straightforward to identify the instant at which the head-end pressure drops and remains below the threshold value p_v in the blowdown stage. The uncertainty can be minimized by employing the following formula to determine the valve-closed time:

$$\tau_{\mathrm{close}} = (1+\varepsilon)\tau_{-1} - \varepsilon\tau_{-2} \tag{14}$$

where τ_{-1} and τ_{-2} are the time periods from the valve close-up to the instants when the head-end pressure drops and remains below the threshold value in each of the previous two cycles, respectively, and ε is a relaxation factor. Clearly, under limit-cycle conditions, $\tau_{\mathrm{close}} = \tau_{-1} = \tau_{-2}$.

Table 3 Nozzle configurations

r_{th}, cm	θ_c	θ_d	$(r_e/r_{\mathrm{th}})^2$
2.0	46.4°	17.3°	6.25
2.5	36.9°	14.5°	4.00
3.0	28.1°	11.6°	2.78
3.5	20.0°	8.69°	2.04
4.0	12.7°	5.78°	1.56
4.5	6.02°	2.88°	1.23
5.0	0.00°	0.00°	1.00

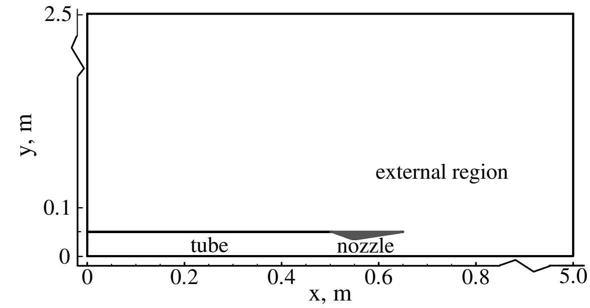

Fig. 3 Computational domain.

C. Boundary and Initial Conditions

The boundary conditions for the detonation tube are specified according to the local flow conditions. The head end is modeled as a rigid wall when the valve is closed. During the purging stage, the total temperature and total pressure (T_{t1}, p_{t1}) are specified, the air mass fraction is set to unity, and the axial velocity is extrapolated from interior points. The same conditions are used during the filling stage, except that the mass fraction of reactants is set to unity. All the solid walls are assumed to be adiabatic. The vertical velocity and normal gradients of the axial velocity, pressure, temperature, and species mass fractions are set to zero at the centerline because of flow symmetry. Along the open boundary of the external region, either a nonreflecting or a fixed-pressure condition can be implemented. Numerical experiments have revealed that these two conditions lead to almost identical flow evolution and system performance if the external region is sufficiently large.

The detonation tube is initially filled with a stoichiometric hydrogen/air mixture at the ambient pressure and temperature, and the nozzle with quiescent air at the same condition. The effect of ambient flow has been investigated in [3]. In spite of its strong interaction with the engine exhaust flow, the ambient flow exerts nearly no influence on the engine propulsive performance and is ignored in the present study. The external region is initially filled with quiescent air.

D. Parameter Space

It is clear from the preceding discussions that a vast degree of freedom exists in the design of a PDE for a specific flight condition. To facilitate system optimization and to identify those key parameters dictating engine performance, the length and inlet/outlet radii of the nozzle, as well as the detonation-tube geometry, are fixed. The remaining operating and geometric parameters are listed as follows. For operation timing: τ_{close}, τ_{purge}, τ_{fill} (external modes), and p_v, β_p, β_f (internal modes); flow conditions at combustor entrance: T_{t1}, p_{t1}; ambient conditions: p_∞, T_∞; and nozzle throat radius: r_{th}.

The engine operation requires three independent control parameters. For an external mode of operation, these three parameters need to be optimized concurrently to obtain the best performance for a given configuration. As for an internal mode, the maximum performance always occurs when the threshold pressure equals the total pressure at the combustor entrance. Only two parameters need to be optimized, and the performance optimization process is greatly simplified.

IV. Numerical Framework

The theoretical formulation is based on the conservation equations of mass, momentum, energy, and species concentration in axisymmetric coordinates. Diffusive effects are neglected because of their minor roles in determining the overall flow dynamics and propulsive performance of a PDE. The resultant governing equations can be written in the following vector form:

$$\frac{\partial \boldsymbol{Q}}{\partial t} + \frac{\partial \boldsymbol{E}}{\partial x} + \frac{\partial \boldsymbol{F}}{\partial y} = \boldsymbol{H} \tag{15}$$

where the dependent variable vector $\boldsymbol{Q}$, convective flux vectors $\boldsymbol{E}$ and $\boldsymbol{F}$, and source vector $\boldsymbol{H}$ are defined as

$$\boldsymbol{Q} = \begin{bmatrix} \rho \\ \rho u \\ \rho v \\ \rho e_t \\ \rho Z_i \end{bmatrix}, \qquad \boldsymbol{E} = \begin{bmatrix} \rho u \\ \rho u^2 + p \\ \rho uv \\ u(\rho e_t + p) \\ \rho u Z_i \end{bmatrix}$$
$$\boldsymbol{F} = \begin{bmatrix} \rho v \\ \rho uv \\ \rho v^2 + p \\ v(\rho e_t + p) \\ \rho v Z_i \end{bmatrix}, \qquad \boldsymbol{H} = \begin{bmatrix} 0 \\ 0 \\ 0 \\ 0 \\ \dot{\omega}_i \end{bmatrix} - \frac{1}{y}\begin{bmatrix} \rho v \\ \rho uv \\ \rho v^2 \\ v(\rho e_t + p) \\ \rho v Z_i \end{bmatrix} \tag{16}$$

Three nominal species are employed herein, namely, reactants (i.e., the stoichiometric H_2/air mixture), detonation products, and air. The chemical kinetics is modeled by a one-step, irreversible reaction expressed with a single progress variable. The mass production rates of reactants and products are, respectively,

$$\dot{\omega}_1 = -A\rho Z_1 \exp(-T_a/T) \tag{17}$$

$$\dot{\omega}_2 = -(W_2/W_1)\dot{\omega}_1 \tag{18}$$

The pressure p and temperature T are obtained through the equations of state:

$$p = (\gamma - 1)\rho[e_t - (u^2 + v^2)/2 - Z_1 q] \tag{19}$$

$$T = p/(\rho R) \tag{20}$$

The gas constant R and specific heat ratio γ of the mixture are calculated as

$$R = \sum Z_i R_i \tag{21}$$

$$\gamma = \frac{\sum Z_i R_i \gamma_i/(\gamma_i - 1)}{\sum Z_i R_i/(\gamma_i - 1)} \tag{22}$$

with the summation over all species.

A total of nine model parameters are involved in the formulation: the specific heat ratios and gas constants of the reactant, product, and air (i.e., γ_i and R_i, $i = 1, 2, 3$), the heat release of reactant q, the preexponential factor A, and the activation temperature T_a. Their values are summarized in Table 4 and discussed in the following paragraphs.

The thermodynamic parameters (γ_i, R_i, and q) are optimized to faithfully predict the detonation wave speed and CJ properties within the range of initial pressure and temperature of interest. For a given reactant pressure p_1 and temperature T_1, the specific heat ratios and gas constants of the reactant and product, as well as the CJ pressure p_2 and temperature T_2 and detonation speed u_D can be readily obtained from a chemical-equilibrium analysis [31]. The equivalent heat release is then calculated as

$$q = \left(\frac{\gamma_2}{\gamma_2 - 1} R_2 T_2 + \frac{1}{2}\gamma_2 R_2 T_2\right) - \left(\frac{\gamma_1}{\gamma_1 - 1} R_1 T_1 + \frac{1}{2} u_D^2\right) \tag{23}$$

This ensures that the analytical CJ properties, expressed by the following equations, exactly match those from the chemical-equilibrium calculation:

$$\frac{p_2}{p_1} = \frac{1 + \gamma_1 M_D^2}{1 + \gamma_2} \tag{24}$$

$$\frac{T_2}{T_1} = \frac{R_1}{R_2}\frac{\gamma_2}{\gamma_1}\left[\frac{1 + \gamma_1 M_D^2}{(1 + \gamma_2) M_D}\right]^2 \tag{25}$$

Table 4 Model parameters for detonation of stoichiometric hydrogen-air mixture

Model parameter	Value
γ_1 (reactant)	1.3961
γ_2 (product)	1.1653
γ_3 (air)	1.4
R_1, J/kg-K	395.75
R_2, J/kg-K	346.2
R_3, J/kg-K	287.00
q, MJ/kg	5.4704
T_a, K	15,100
A, 1/s	1.0×10^9

$$M_D = \sqrt{\left(\frac{\gamma_2^2 - 1}{\gamma_1}\frac{q}{R_1 T_1} + \frac{\gamma_2^2 - \gamma_1}{\gamma_1^2 - \gamma_1}\right) + \sqrt{\left(\frac{\gamma_2^2 - 1}{\gamma_1}\frac{q}{R_1 T_1} + \frac{\gamma_2^2 - \gamma_1}{\gamma_1^2 - \gamma_1}\right)^2 - \left(\frac{\gamma_2}{\gamma_1}\right)^2}} \tag{26}$$

In the present work, the reference state for the reactant is chosen to be 2 atm and 400 K, close to that of the filled reactant for the baseline flight condition with an altitude of $h = 9.3$ km and Mach number of $M_\infty = 2.1$. The maximum relative errors of the CJ pressure, temperature, and detonation wave speed are 3, 5, and 2%, respectively, over the initial pressures of 1–8 atm and initial temperatures of 300–800 K. The errors decrease as the initial condition approaches the reference point and become less than 1% for typical filled reactant conditions associated with the flight conditions considered herein.

The chemical kinetic parameters of the preexponential factor A and activation temperature T_a affect the internal structure of a detonation wave front and should be selected in a manner consistent with numerical resolution [32]. For a system-level analysis of PDE performance, it appears unnecessary to resolve the details within a detonation wave front at the expense of excessive computer resources. The transverse motion associated with the cellular structures at the wave front may divert some of the axial impulse to its transverse counterpart. An order-of-magnitude analysis, however, indicates that the kinetic energy of transverse oscillations represents an exceedingly small fraction of the potential and kinetic energies of the detonation wave. The impact of those fine structures to the engine propulsive performance can thus be ignored. Without loss of generality, the activation energy is fixed at a common value of 30 kcal/mol, and the corresponding activation temperature is

$$T_a = \frac{E_a}{R_u} = \frac{30,000 \times 4.184}{8.314} = 15,097 \approx 15,100 \text{ K} \tag{27}$$

The preexponential factor A is determined from a series of calculations of one-dimensional detonation initiation and propagation. The detonation tube measures 40 cm long, with a driver gas region of 0.4 cm near the head end. The grid size is fixed at $dx = 1$ mm. The tube is initially filled with a stoichiometric H_2-air mixture at 2 atm and 400 K and a driver gas at 40 atm and 4000 K. The lower limit $A_{\min}$ of 5.6×10^8 s^{-1} is obtained by gradually decreasing A until detonation cannot be initiated, whereas the upper limit $A_{\max}$ of 1.9×10^9 s^{-1} is obtained by increasing A until the detonation wave becomes an unphysical wave that propagates at a speed determined by the numerical grid size and time step rather than the CJ detonation speed. The optimum value of A for a prespecified grid size is taken to be the geometrical mean

$$A = \sqrt{A_{\min} A_{\max}} \tag{28}$$

Correspondingly, based on the discussion of the scaling issue by Choi et al. [32], the requirement on the grid size for a given A that is optimized for a grid size dx is

$$dx \cdot A_{\min}/A \sim dx \cdot A_{\max}/A \tag{29}$$

The theoretical formulation outlined above is solved numerically using the space-time conservation element/solution element method [33,34]. This scheme offers many unique features, such as a unified treatment of space and time, introduction of solution and conservation elements to construct a simple stencil, treatment of dependent variables and their derivatives as unknowns to be solved simultaneously, and no interpolation or extrapolation required to evaluate fluxes at cell interfaces. Furthermore, it has extremely low numerical dissipation and dispersion errors, rendering the scheme very effective in treating detonation waves and shock discontinuities. The resultant computer code is further parallelized using the message-passing-interface library and a domain-decomposition technique for unstructured grids [35]. The entire analysis has been validated against a series of detonation problems for which either analytical solutions or experimental data are available [3,4,17,34].

V. Analytical Models of Engine Performance

Because of the flow unsteadiness and complexity inherent in PDE operation, the engine propulsive performance in general cannot be accurately predicted by analytical means. On the other hand, it is desirable to develop simple analytical models to assess the theoretical limit of PDE performance and to identify various performance loss mechanisms. Several models have been proposed and can be classified into two categories. The first group uses unsteady gasdynamics theories to determine the system performance based on the pressure at the closed end of a detonation tube [5,36]. Owing to the various approximations employed, the approach is primarily applied to straight detonation tubes with single-pulse operations, for which a semi-closed-form solution is available. The second group extends classical thermodynamic cycle analyses for steady-flow engines to accommodate unique features of PDE operation [3,17,20,21]. The analytical model developed in the present study falls into this category.

Following the general concept outlined by Heiser and Pratt [20], we consider the state changes of the working fluid during each cycle of engine operation. Figure 4 shows schematically the flowpath studied in the analysis, where the subscripts ∞, 1, 2, and e represent the states of the freestream, unburned gas, CJ point, and exit plane, respectively. The effects of inlet loss, filling velocity, and purging process are taken into account [3]. The procedure for performance prediction is summarized as follows:

1) Determine the total temperature T_{t1} and pressure p_{t1} at the combustor entrance from the inlet flow analysis.

2) Obtain the static temperature T_1 and pressure p_1 of reactants for a given filling Mach number M_1:

$$T_1 = T_{t1} \Big/ \left[1 + (\gamma_1 - 1) M_1^2/2\right] \tag{30}$$

$$p_1 = p_{t1} \Big/ \left[1 + (\gamma_1 - 1) M_1^2/2\right]^{\gamma_1/(\gamma_1 - 1)} \tag{31}$$

3) Calculate the CJ temperature T_2 and pressure p_2 using Eqs. (25) and (24).

4) Calculate the exit temperature by assuming isentropic flow expansion from the CJ state to the exit plane as well as a perfect match of the exit pressure with the ambient value,

$$T_e = T_2 (p_\infty/p_2)^{(\gamma_2 - 1)/\gamma_2} \tag{32}$$

5) Deduce the exit velocity by applying the energy balance between the combustor entrance and the nozzle exit,

$$u_e = \sqrt{2[q - (c_{p2} T_e - c_{p1} T_{t1})]} \tag{33}$$

6) Determine the specific impulse from

$$I_{\mathrm{sp}} = \frac{(1+f) u_e - u_\infty}{f g} \tag{34}$$

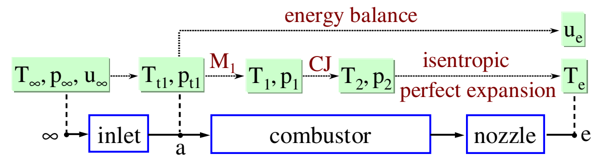

Fig. 4 Schematic of flowpath analysis for PDE performance prediction ([3]).

The effect of purge gas can be easily accommodated. The resultant exit temperature can now be determined based on the following average:

$$T_e = T_{e1}\beta + T_{e2}(1-\beta) \tag{35}$$

where β is defined as the ratio of the purge to the valve-open time period,

$$\beta = \tau_{\mathrm{purge}}/\tau_{\mathrm{open}} \tag{36}$$

and T_{e1} and T_{e2} are the temperatures obtained by assuming isentropic flow expansion from the purge-gas state (T_1, p_1) and the CJ state (T_2, p_2) to the exit plane, respectively,

$$T_{e1} = T_1 (p_\infty/p_1)^{(\gamma_\infty - 1)/\gamma_\infty}, \qquad T_{e2} = T_2 (p_\infty/p_2)^{(\gamma_2 - 1)/\gamma_2} \tag{37}$$

The heat addition q in Eq. (33) and the fuel-to-air mass ratio f in Eq. (34) should be replaced by their respective overall quantities:

$$\tilde{q} = q \cdot \tau_{\mathrm{fill}}/\tau_{\mathrm{open}} = q(1-\beta) \tag{38}$$

$$\tilde{f} = f \cdot \tau_{\mathrm{fill}}/\tau_{\mathrm{open}} = f(1-\beta) \tag{39}$$

The input parameters in the present analysis include q, f, u_∞, T_∞, p_∞, p_{t1}, M_1, and β, in addition to the specific-heat ratios and gas constants. Note that the stagnation temperature T_{t1} is a function of u_∞ and T_∞.

The same analysis can also be applied to predict the performance of a ramjet engine with constant-pressure combustion, except that the temperature and pressure of combustion products in step 3 are replaced by the following:

$$T_2 = (c_{p1} T_1 + q)/c_{p2} \tag{40}$$

$$p_2 = p_1 \tag{41}$$

In the limiting case in which the effects of inlet loss, filling Mach number, and purge time are ignored, the thermodynamic cycle efficiency, defined as the percentage of the heat released from chemical reactions that is converted to kinetic energy, of an ideal PDE becomes [37]

$$\eta_{\mathrm{th,PDE}} = 1 - \frac{1}{q/(c_{p\infty} T_\infty)} \left[\frac{(\gamma_\infty - 1)}{(\gamma_2 - 1)} \cdot \frac{\gamma_2^2}{\gamma_\infty \gamma_1} \cdot \frac{R_1}{R_\infty} \cdot \frac{1}{M_D^2} \left(\frac{1 + \gamma_1 M_D^2}{1 + \gamma_2} \right)^{\frac{\gamma_2 + 1}{\gamma_2}} \left(\frac{T_1}{T_\infty} \right)^{1 - \frac{\gamma_2 - 1}{\gamma_\infty - 1} \frac{\gamma_\infty}{\gamma_2}} - 1 \right] \tag{42}$$

The efficiencies of the corresponding Brayton and Humphrey cycles are

$$\eta_{\mathrm{th,Brayton}} = 1 - \frac{1}{q/(c_{p\infty} T_\infty)} \left[\frac{\gamma_1(\gamma_\infty - 1)}{\gamma_\infty(\gamma_1 - 1)} \cdot \frac{R_1}{R_\infty} \cdot \left(\frac{q}{c_{p1} T_1} + 1 \right) \left(\frac{T_1}{T_\infty} \right)^{1 - \frac{\gamma_2 - 1}{\gamma_\infty - 1} \frac{\gamma_\infty}{\gamma_2}} - 1 \right] \tag{43}$$

$$\eta_{\mathrm{th,Humphrey}} = 1 - \frac{1}{q/(c_{p\infty}T_\infty)}\left[\frac{\gamma_1(\gamma_\infty - 1)}{\gamma_\infty(\gamma_1 - 1)}\cdot\frac{R_1}{R_\infty}\right.$$
$$\left.\cdot\frac{\gamma_2}{\gamma_1}\left(\frac{\gamma_1 - 1}{\gamma_2 - 1}\right)^{\frac{\gamma_2 - 1}{\gamma_2}}\left(\frac{\gamma_1 q}{c_{p1}T_1} + 1\right)^{\frac{1}{\gamma_2}}\left(\frac{T_1}{T_\infty}\right)^{1 - \frac{\gamma_2 - 1}{\gamma_\infty - 1}\frac{\gamma_\infty}{\gamma_2}} - 1\right] \tag{44}$$

Finally, the specific impulse can be determined from the following equation:

$$I_{\mathrm{sp}} = \frac{(1+f)\sqrt{u_\infty^2 + 2[\eta_{\mathrm{th}} q + (c_{p1} - c_{p\infty})T_1]} - u_\infty}{fg} \tag{45}$$

The above thermodynamic cycle analysis requires input parameters of q, f, u_∞, and T_∞ as well as the specific-heat ratios and gas constants at different states. The stagnation temperature at the combustor entrance is determined from the freestream condition. Equations (42–45) reduce to those given in [20] if variations of thermophysical properties at various states are ignored.

VI. Results and Discussion

A series of simulations are conducted to assess the engine performance at given flight conditions using both the external and internal modes of valve operation. In the external control mode, the timing sequence of valve operation is prespecified. Efforts are first applied to study the flow evolution, propulsive performance, and loss mechanisms for the baseline case with a flight altitude of $h = 9.3$ km and Mach number of $M_\infty = 2.1$. The effect of valve timing on performance is then examined systematically. In the internal control mode, the valve operation depends on the flow development in the detonation tube. The effect of filling fraction is first studied. Results are then used as a basis on which the dependence of engine performance on nozzle configuration and flight condition is investigated. The analytical performance analysis outlined in Sec. V is also applied to determine the theoretical limit of PDE performance.

A. External Control of Valve Operation

1. Flow Evolution for Baseline Case

The baseline flight condition involves an altitude of $h = 9.3$ km and Mach number of $M_\infty = 2.1$, which has been previously studied by the authors [3,4] and later by Harris et al. [18] using a single- and a multiple-γ model, respectively. The nozzle throat radius is selected to be 3.5 cm, and the operation timing is set for a cycle period (τ_{cycle}) of 4 ms, a valve-closed time (τ_{close}) of 3.0 ms, and a purge time (τ_{purge}) of 0.1 ms. The calculation takes about seven cycles to reach a steady cyclic (i.e., limit-cycle) operation.

Figure 5 shows the temporal evolution of the density-gradient field during the first and a steady cycle. Initially, the detonation tube is closed and filled with a stoichiometric hydrogen/air mixture at the ambient pressure (0.29 atm) and temperature (228 K), and the nozzle and external region with quiescent ambient air. Detonation is directly initiated by a driver gas at 4000 K and 40 atm, spanning a length of 0.05 cm from the head end. The associated initiation energy, which is about 0.7% of the chemical energy of the reactant, has a negligible contribution to the engine impulse [3]. The detonation wave then propagates downstream and degenerates to a nonreacting shock wave after passing through the reactant/air interface at the tube exit. The resultant primary shock wave proceeds further downstream and reflects from the nozzle walls, leading to a complex flow structure. Typical flow features include the expanding primary shock, shear layers, Prandtl–Meyer expansion fan originating from the edge of the nozzle exit at the initial stage of the blowdown phase and oblique or normal shock in the later blowdown process, and numerous reflected shock waves. The flow evolution is qualitatively similar to what has been extensively discussed in [3]. Details will not be repeated here.

The development of the wave structure can be clearly revealed by an x–t diagram, which is obtained by recording the eigenvalues (i.e., u, $u + c$, and $u - c$) along the centerline of the chamber and then constructing the "streamlines" in the x–t domain based on the "velocity vectors" of $(u, 1)$, $(u + c, 1)$, and $(u - c, 1)$ [37]. Figure 6 shows the result of the first cycle as well as the time histories of flow properties at the head end and nozzle exit. The detonation wave, as indicated by the dense black line, propagates downstream through the unburned mixture (region 1) at a CJ velocity of 1974 m/s, followed by the Taylor expansion waves (region 2), and a uniform region (region 3).

The detonation wave reaches the reactant/air interface at the tube exit at $t = 0.253$ ms (point A) and then degenerates to a nonreacting shock (i.e., the primary shock wave). Both the primary shock and the contact surface proceed further downstream into the nozzle and external region. Meanwhile, a reflected shock and a series of compression/expansion waves are produced and propagate upstream, resulting in a nonsimple wave region (region 4) when interacting with the downstream-traveling Taylor waves. A simple wave region (region 5) is recovered after these waves pass through the Taylor waves. The reflected shock reaches the head end at $t = 0.740$ ms (point B), giving rise to a jump in the head-end pressure.

Within the nozzle, a sonic region is formed at about $x = 0.56$ m shortly after the passing of the primary shock wave, as evidenced by the clustered vertical characteristic lines in the x–t diagram. The sonic point is located slightly downstream of the nozzle throat at $x = 0.55$ m. This phenomenon may be attributed to the fact that the sonic line in a multidimensional nozzle flowfield is curved, starting at the wall slightly upstream of the throat and crossing the nozzle centerline downstream of the throat [3,38]. After the sonic region, the flow is expanded to become supersonic and finally a secondary shock is formed in the divergent section. As this shock is swept further downstream by the flow, its strength weakens and the flow downstream of it becomes supersonic again. Another secondary shock is later formed in the external region to match the subsonic flow behind the primary shock. The two secondary shock waves are clearly seen in the snapshot of 0.80 ms in Fig. 5, one at $x = 0.68$ m and the other at $x = 0.76$ m. Further interactions between the waves and the multidimensional effect render the characteristic lines more complex. As the blowdown process continues, the flow is overexpanded by the nozzle, and a nearly normal shock is formed near the nozzle exit, which is evidenced by the dense lines in the snapshots of 3.0, 3.1, and 3.4 ms in Fig. 5. The continuous movement of this shock is indicated by the corresponding lines in the x–t diagram.

The head-end pressure decays to 0.58 atm at $t = 3.0$ ms when the valve opens and the purging stage begins, whereas the total pressure at the combustor entrance is 2.30 atm. Because of the pressure difference across the valve, a right-running shock wave is established, along with a contact surface between the product and the purge air. Another contact surface forms between the fresh reactant and purge air when the filling stage commences at 0.1 ms later. The filling velocity and Mach number at the head end are about 435 m/s and 0.96, respectively. In the region from the head end through the air/product contact surface, the flow becomes slightly supersonic due to the expansion waves arising from the downstream region.

Figure 7 shows the x–t diagram and time histories of flow properties in a limit (i.e., the seventh) cycle. The main flow features such as the primary shock wave, Taylor waves, and reflected shock waves remain qualitatively the same as those in the first cycle. The detonation wave catches the reactant/air contact surface at about $x = 0.43$ m, slightly upstream of the tube exit as in the first cycle. The secondary shock waves disappear because the flow behind the primary shock wave is already supersonic. The variation in the head-end pressure becomes more complicated due to the influence of the previous cycle. The arrival and formation of shocks at the head end are denoted by the filled square symbols in the x–t diagram. Points s_1 and s_2 are associated with the shocks from the previous cycle, points s_3, s_4, and s_5 with the reflected shocks, and point s_6 with the valve-opening induced shock. The time-averaged filling pressure, velocity, and Mach number at the head end in a limit cycle are 1.57 atm, 349 m/s, and 0.76, respectively. The filling velocity is considerably lower than that of the first cycle.

2. Propulsive Performance of Baseline Case

The engine specific impulse, specific thrust, and net thrust can be determined using Eqs. (1), (2), and (7) detailed in Sec. II. Figure 8 shows the temporal variation of the specific impulse during the first eight cycles for the baseline case. The low value of the first cycle is attributed to the initial filling of reactants at the ambient pressure, which is much lower than the chamber pressure in later cycles. The specific impulse reaches a steady value of 4773 s at about the seventh cycle.

3. Performance Loss Mechanisms of Baseline Case

The performance loss mechanisms in an airbreathing PDE were examined in our previous work using a single-γ model [3]. In addition to flow losses in the inlet and manifold, several performance degradation mechanisms in the combustor and nozzle were identified and quantified. These include viscous damping, wall heat transfer, filling process, nozzle flow expansion and divergence, and internal-flow process. The filling loss is mainly attributed to the decrease of reactant pressure with increasing filling velocity. The nozzle-expansion loss is due to the mismatch of the exit pressure with the ambient state. The nozzle-divergence loss results from the angularity of the exhaust velocity vector. The internal-flow loss is associated with the complicated waves (especially the shock waves) within the chamber.

To quantify the various loss mechanisms, the analytical analysis detailed in Sec. V is first employed to predict the theoretical limit of the engine performance in terms of the flow, geometric, and operation parameters, $q, f, u_\infty, T_\infty, p_\infty, p_{t1}, M_1$, and β, as well as the specific-heat ratios and gas constants. For the baseline case, the filling Mach number M_1 is taken from the numerical result of 0.76. Other parameters remain identical to those in the numerical simulation, with $p_{t1} = 2.30$ atm and $\beta = 0.1$. The resultant analytical prediction of the specific impulse is 5147 s, about 7.8% higher than the calculated value of 4773 s. The discrepancy results from the underlying assumptions adopted in the analytical model, including the steady-state flow condition at the engine exit, uniform flow properties of the filled reactant, isentropic flow expansion from the CJ state to the exit plane, perfect match with the ambient pressure at the nozzle exit, and uniform exhaust flow in parallel to the nozzle axis. Following the analysis outlined in [3], the nozzle-expansion, nozzle-divergence, and internal-flow losses are estimated to be 5.1, 1.0, and 1.7% (with respect to the numerically calculated value of 4773 s), respectively. If the filling Mach number M_1 is set to zero, the analytically predicted specific impulse becomes 5382 s. The difference from that with $M_1 = 0.76$ accounts for a performance loss

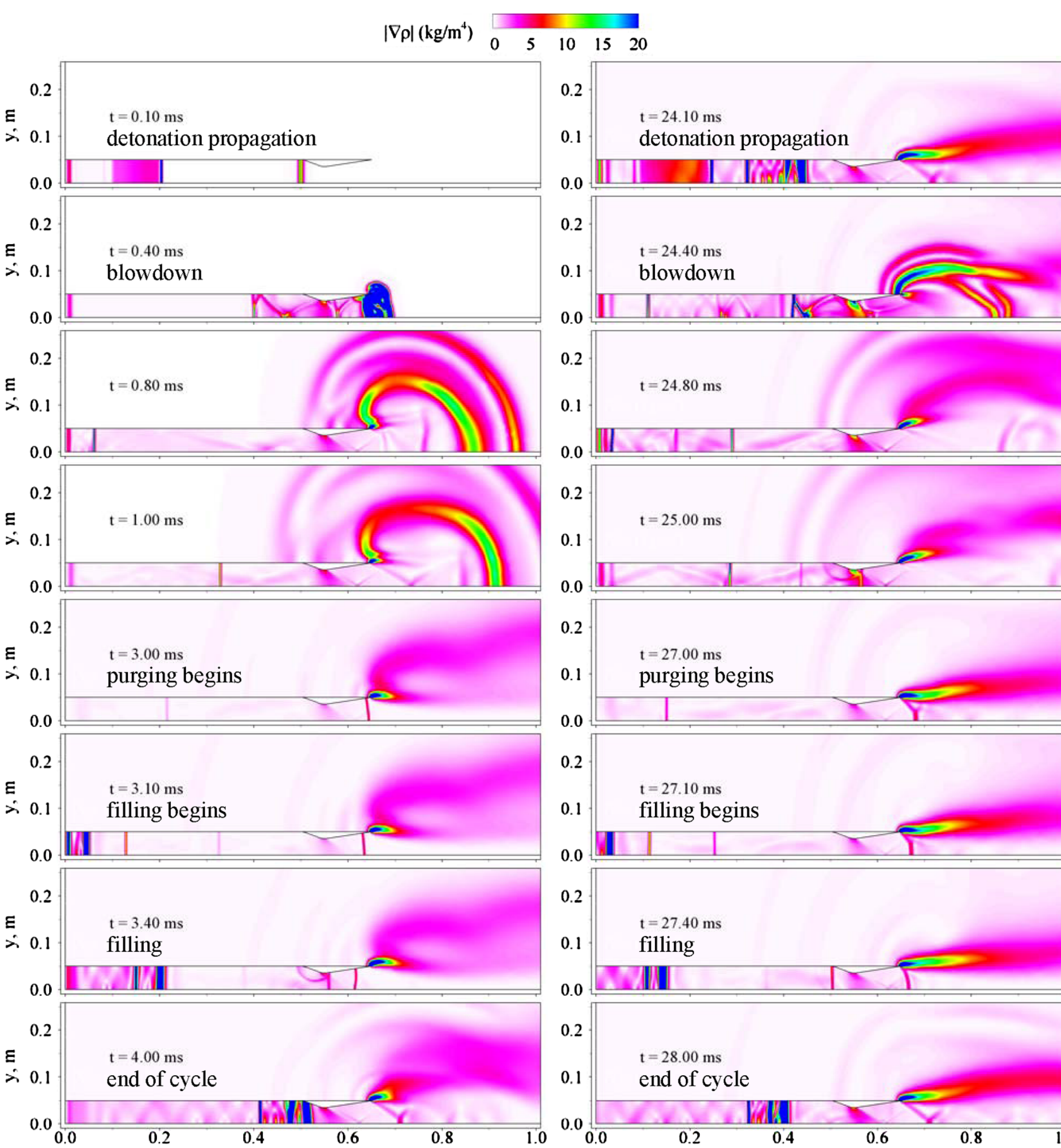

Fig. 5 Time evolution of density-gradient field during first (left) and seventh (right) cycles; $\tau_{cycle} = 4$ ms, $\tau_{close} = 3.0$ ms, $\tau_{purge} = 0.1$ ms for stoichiometric H_2/air mixture at $h = 9.3$ km and $M_\infty = 2.1$.

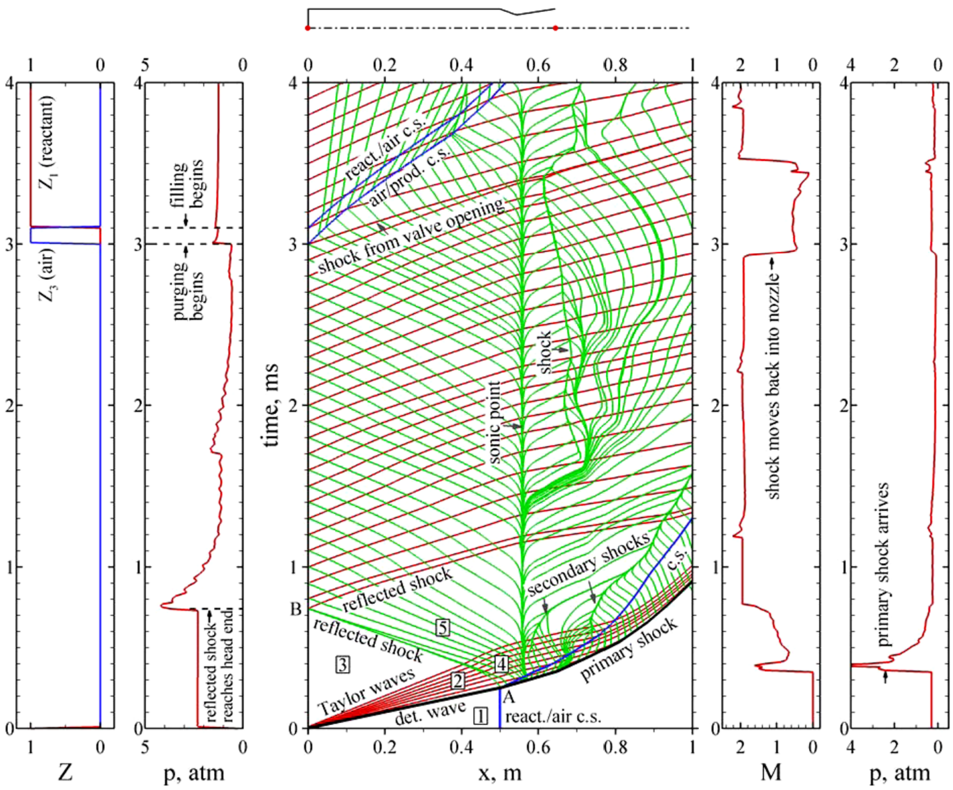

Fig. 6 ***x–t*** **diagram (middle) and time histories of flow properties at tube head end (left) and nozzle exit (right) for first cycle; $\tau_{\text{cycle}} = 4$ ms, $\tau_{\text{close}} = 3.0$ ms, $\tau_{\text{purge}} = 0.1$ ms for stoichiometric H_2/air mixture at $h = 9.3$ km and $M_\infty = 2.1$; 1 = unburned region, 2 = Taylor expansion waves, 3 = stationary region, 4 = nonsimple wave region, 5 = simple wave region.**

of 4.4% (with respect to the analytical value of 5382 s) due to the filling velocity. The other three losses associated with exhaust-flow expansion, nozzle-divergence, and internal-flow processes then become 4.8, 0.9, and 1.6%, respectively.

Quite interestingly, the internal-flow loss in the current case is very small in spite of the existence of strong shock waves within the internal flowfield. This can be explained as follows. The internal-flow loss is obtained by comparing the numerical result with the

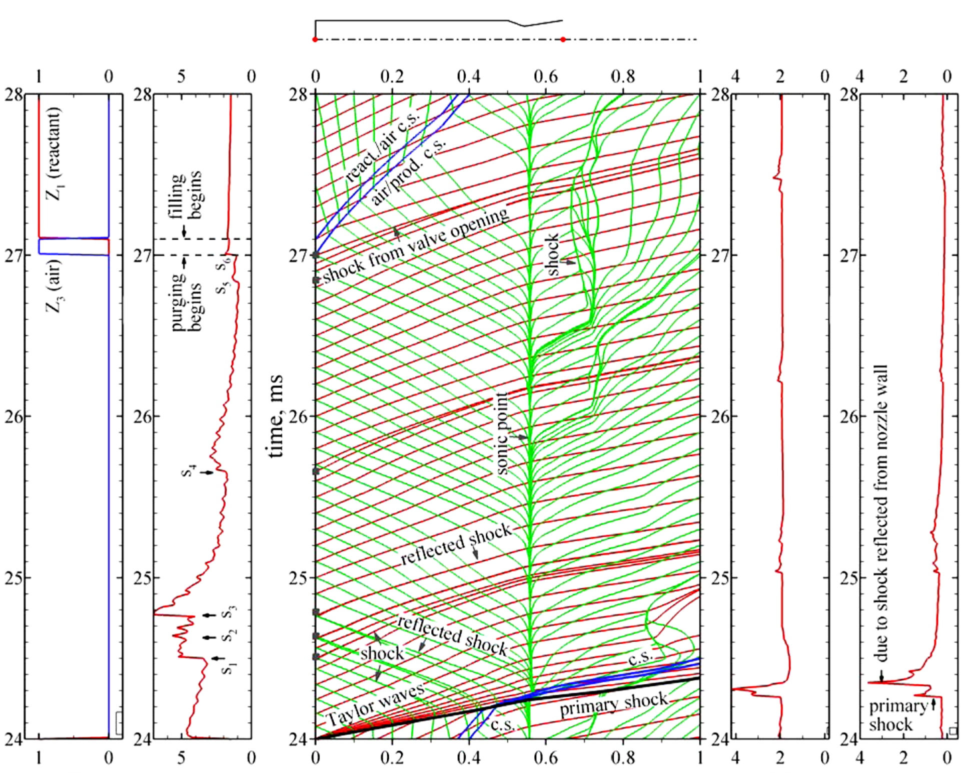

Fig. 7 ***x–t*** **diagram (middle) and time histories of flow properties at tube head end (left) and nozzle exit (right) for seventh cycle; $\tau_{\text{cycle}} = 4$ ms, $\tau_{\text{close}} = 3.0$ ms, $\tau_{\text{purge}} = 0.1$ ms for stoichiometric H_2/air mixture at $h = 9.3$ km and $M_\infty = 2.1$.**

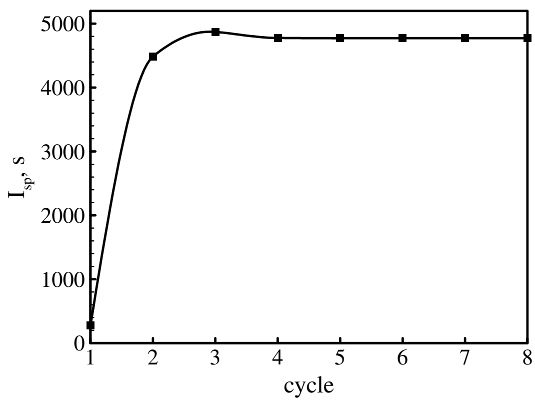

Fig. 8 Temporal variation of specific impulse during first eight cycles; $\tau_{cycle} = 4$ ms, $\tau_{close} = 3.0$ ms, $\tau_{purge} = 0.1$ ms for stoichiometric H_2/air mixture at $h = 9.3$ km and $M_\infty = 2.1$.

analytical prediction and subtracting the nozzle expansion and divergence losses from the total loss. Three aspects should be noted. First, in the analytical model, the flow is assumed to undergo an isentropic expansion from the CJ state to the exit plane, while in reality complicated shock waves exist within the chamber and the corresponding entropy rise leads to certain performance loss. Second, the filled reactants have uniform properties in the analytical model. They are, however, influenced by expansion and other waves in a real flow environment. This kind of loss can also be regarded as part of the filling loss by taking the reactant Mach number before the arrival of the detonation wave as the filling Mach number. Third, the analytical model assumes a steady exit flow, which in reality does not occur. The correlation between the instantaneous velocity and mass flow rate may either enhance or weaken the exhaust momentum and thus the performance, as also pointed out by Cambier and Tegner [16]. Therefore, the internal-flow loss may become small if the performance gain from the density-velocity correlation offsets the losses from the other two factors.

4. *Effect of Valve Timing*

The effect of valve timing on the engine propulsive performance is studied over a broad range of cycle τ_{cycle} and valve-closed τ_{close} times. The purge time τ_{purge} is fixed at 0.1 ms as in the baseline case. Figure 9 shows the influence of τ_{close} on the specific impulse I_{sp} for three different cycle periods of 3, 4, and 5 ms. The corresponding operating frequencies are 333, 250, and 200 Hz, respectively. There exist two lower bounds of τ_{close}, one associated with inlet overpressurization (denoted by open circles) and the other with combustor overfilling (denoted by filled circles) [3]. Steady cyclic operation is achieved after 5–20 cycles in these cases. The performance trend is similar to that discussed in [3]. The specific impulse increases as τ_{close} decreases for a given frequency, except for a small range near the lower bound. For the three frequencies considered herein, the 250 Hz ($\tau_{cycle} = 4$ ms) operation offers the best performance margin. The maximum specific impulse of 4925 s is obtained with $\tau_{close} = 2.7$ ms, which is 3.2% higher than that of the baseline case with $\tau_{close} = 3.0$ ms.

B. Internal Control of Valve Operation

As discussed in Sec. II, the valve timing can also be controlled internally by the threshold pressure, purge fraction, and filling fraction, based on the flow development in the chamber. Intuitively, the specific impulse and thrust increase with increasing threshold pressure and reach their maxima when the threshold pressure equals the total pressure at the combustor entrance (p_{t1}). On the other hand, at this maximum threshold pressure, the purging/filling processes may proceed slowly, leading to a low operating frequency. With these in mind, the threshold pressure is fixed at 95% of the total pressure (p_{t1}) in the present study to achieve a reasonable performance. The effect of purge fraction resembles that of purge time discussed in [3]. The specific impulse increases but the specific thrust decreases with increasing purge time for given cycle and valve-open times, a phenomenon similar to the bypass-air effect for conventional gas-turbine engines. The specific value of purge fraction depends on the relative importance of specific impulse and thrust in the engine design. For simplicity, the purge fraction is set to a small value of 0.02, sufficient to prevent preignition while exerting a negligible influence on the specific impulse. In reality, a relatively larger value may be required to provide a wider safety margin accommodating the various instabilities arising from the contact surfaces and shock waves. With the above prespecifications, only one parameter, that is, the filling fraction β_f, remains to be optimized, as opposed to two parameters (i.e., τ_{cycle} and τ_{close}) in the external control mode with a fixed τ_{purge}. The entire engine optimization procedure can thus be substantially expedited.

1. *Effect of Filling Fraction*

The effect of a filling fraction on engine propulsive performance is first studied for the baseline flight condition with $M_\infty = 2.1$ and $h = 9.3$ km. The threshold pressure and purge fraction are set to 2.19 atm and 0.02, respectively. Figure 10 shows the specific impulse and period of each cycle with a filling fraction of 0.8. The cycle period varies until the steady operation is reached at the 12th cycle. The corresponding specific impulse and cycle time are 4850 s and 4.04 ms, respectively. Figure 11 shows the time histories of the pressure and mass fractions at the head end during limit cycles. The valve opens and the purging process begins when the head-end pressure decays to the prespecified value of 2.19 atm. The pressure continues to decrease during the purging and filling processes due to the expansion waves propagating from the downstream region. The average filling pressure of 2.01 atm is slightly lower than the threshold value. The average filling Mach number is 0.438, and the

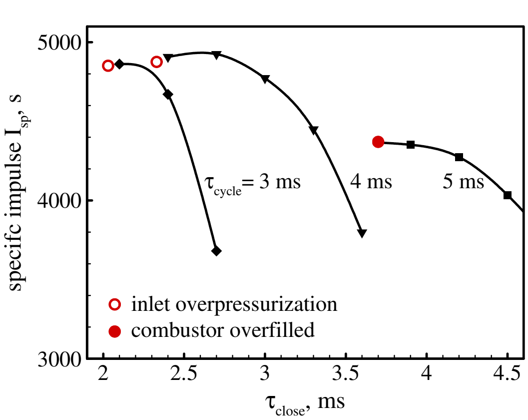

Fig. 9 Effects of valve-closed time on specific impulse I_{sp} for three different operation frequencies; $\tau_{purge} = 0.1$ ms for stoichiometric H_2/air mixture at $h = 9.3$ km and $M_\infty = 2.1$.

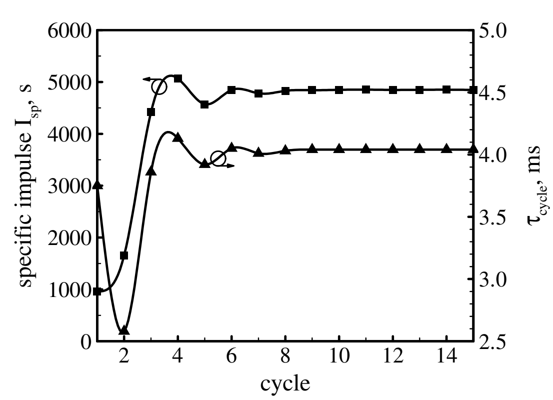

Fig. 10 Specific impulse and period of each cycle; $p_v = 2.19$ atm, $\beta_f = 0.8$, $\beta_p = 0.02$ for stoichiometric H_2/air mixture at $h = 9.3$ km and $M_\infty = 2.1$.

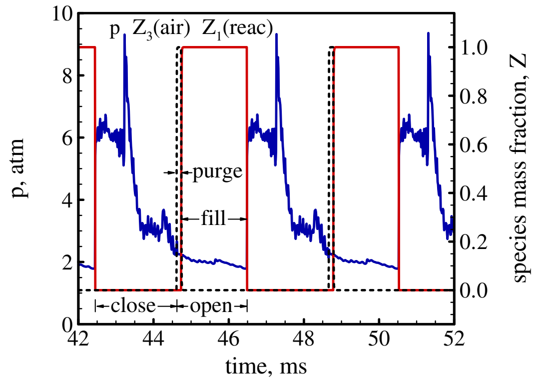

Fig. 11 Time histories of pressure and mass fractions at head end during limit cycles (two full cycles, i.e., 12th and 13th cycles are shown); $p_v = 2.19$ atm, $\beta_f = 0.8$, $\beta_p = 0.02$ for stoichiometric H_2/air mixture at $h = 9.3$ km and $M_\infty = 2.1$.

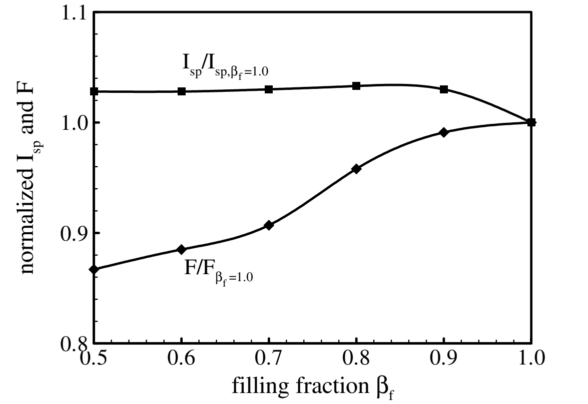

Fig. 13 Normalized specific impulse and thrust as function of filling fraction; $p_v = 2.19$ atm, $\beta_p = 0.02$ for stoichiometric H_2/air mixture at $h = 9.3$ km and $M_\infty = 2.1$.

corresponding theoretical specific impulse is 5200 s. The overall performance loss is broken down to a filling loss of 1.5%, a nozzle-expansion loss of 4.6%, a nozzle-divergence loss of 0.8%, and an internal-flow loss of 1.2%, in reference to the analytical value of 5276 s with zero filling Mach number.

Figure 12 shows the numerically calculated and theoretically predicted specific impulses with various filling fractions. Because the valve opens at the same threshold pressure for all the cases, the filling fraction exerts little influence on the average filling pressure and Mach number, and consequently the propulsive performance. The specific impulse increases by 0.5% when β_f varies from 0.5 to 0.8, and then decreases by about 3.2% when β_f varies from 0.8 to 1.0. The relatively low specific impulse at the filling fraction of 1.0 is due to the incidence of the detonation wave to the leading fresh reactant in the nozzle section and subsequent strong shock reflections within the nozzle. The effect of the filling fraction should not be confused with the partial filling effect reported in the single-pulse studies [39,40], where the specific impulse can be significantly improved by partial filling of reactants in a detonation tube. In a single-pulse operation, the tube contains quiescent cold air that can convert the potential and thermal energies carried by the detonation wave and combustion products to thrust. The situation, however, becomes different in a multicycle operation. The chamber, except for a small amount of purge gas, is already filled with hot combustion products (i.e., residual gases) at either a high subsonic or even a sonic condition. The amount of energy that can be transferred to the residual gases to enhance the efficiency of the nozzle flow expansion appears to be limited.

The effect of a filling fraction on engine thrust and operating frequency was also investigated. Figure 13 shows the thrust and specific impulse (normalized by the corresponding values for $\beta_f = 1$) in the β_f range of 0.5–1.0. The thrust increases monotonically by about 15% with increasing filling fraction from 0.5 to 1.0. This trend can be qualitatively explained as follows. As β_f increases, both the reactant consumed per cycle and the cycle period increase, with the latter occurring at a slower rate. Thus, the overall consumption rate increases with increasing β_f, and so does the thrust. Figure 14 shows the effects of the filling fraction on valve operation times. As the filling fraction increases, both the valve-open time (including the purge and filling durations) and the valve-closed time (including the detonation initiation and propagation as well as blowdown processes) increase. The cycle period increases by 64% as β_f varies from 0.5 to 1.0. The corresponding operating frequency decreases from 358 Hz to 218 Hz.

Based on the above discussions, it is desirable to have the filling fraction in the range of 0.8–0.9 to maximize the specific impulse while maintaining a reasonable thrust. A filling fraction of 0.8 is thus chosen for the remaining calculations. With this selection, only one case needs to be studied for a given configuration, in contrast to the consideration of numerous cases in the external-mode operation for optimizing the valve timing. The performance optimization process is significantly expedited.

2. *Effect of Nozzle Configuration*

A series of nozzle configurations, as shown in Fig. 2 and discussed in Sec. III, are investigated for the baseline flight condition with the Mach number of 2.1 and altitude of 9.3 km. The nozzle throat radius varies from 2.0 to 5.0 cm, and the corresponding throat-to-tube area ratio is 0.16–1.0. The case with 5.0-cm throat radius represents a simple extension of the detonation tube. The threshold pressure, filling fraction, and purge fraction are set to 2.0, 0.8, and 0.02 atm,

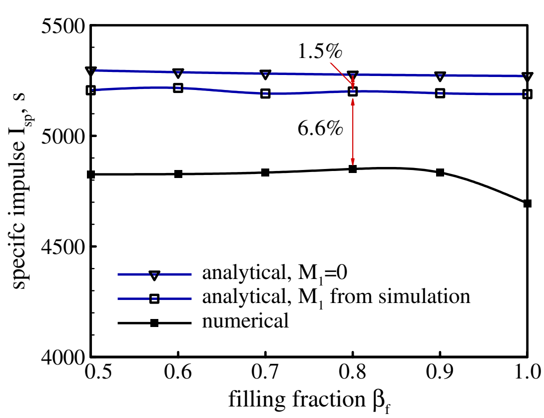

Fig. 12 Effect of filling fraction on specific impulse; $p_v = 2.19$ atm, $\beta_p = 0.02$ for stoichiometric H_2/air mixture at $h = 9.3$ km and $M_\infty = 2.1$, percentage with respect to analytical value of 5276 s.

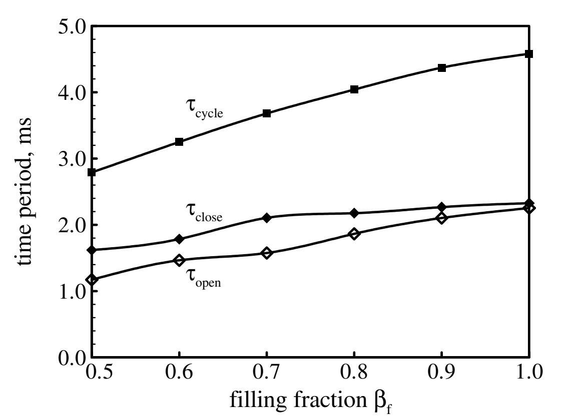

Fig. 14 Effect of filling fraction on valve operation times; $p_v = 2.19$ atm, $\beta_p = 0.02$ for stoichiometric H_2/air mixture at $h = 9.3$ km and $M_\infty = 2.1$.

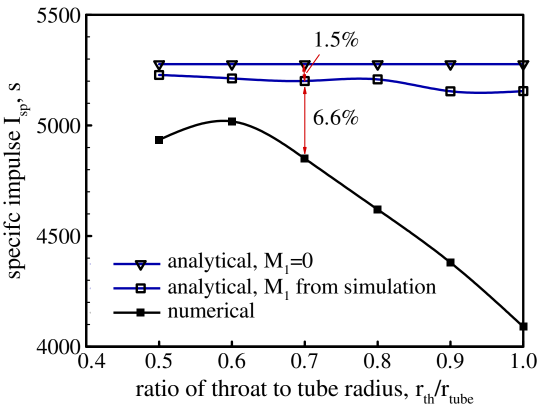

Fig. 15 Effect of nozzle throat area on specific impulse; stoichiometric H_2/air mixture, $h = 9.3$ km, $M_\infty = 2.1$, percentage with respect to analytical value of 5276 s.

respectively, such that only one flow calculation is required for each nozzle configuration.

Figure 15 shows the dependence of the specific impulse on nozzle configuration. The corresponding analytical predictions with the filling Mach number set to zero or based on the numerical result are also included. An optimum nozzle throat area clearly exists at the radius ratio of $r_{th}/r_{tube} = 0.6$. The corresponding specific impulse of 5020 s is about 23% higher than 4090 s of a simple extension of the detonation tube (i.e., $r_{th}/r_{tube} = 1.0$). The result further corroborates the advantages of CD nozzles over straight tubes. The superior performance with a CD nozzle lies in its capability to preserve the chamber pressure during the blowdown and filling processes [3].

Figure 16 shows the effect of the nozzle throat area on various performance losses. As the ratio r_{th}/r_{tube} increases from its optimum value of 0.6 to 1.0, the total performance loss increases from 4.9% to 22% with respect to the theoretically predicted performance. The nozzle-divergence loss decreases due to the decrease in the nozzle-divergence angle. Because the valve opens at a fixed pressure of 2.19 atm for all the cases, the averaged filling pressure only slightly varies with the throat area, and so does the filling loss. The nozzle-expansion loss significantly increases with the throat area, a situation caused by the mismatch of the exit pressure with the ambient condition. Interestingly, the internal-flow loss also increases. As already mentioned, such loss results from the entropy rise associated with shock waves, the decrease of reactant pressure by expansion waves, and the nonlinear correlation between the density and velocity at the exit plane. As the throat area increases, although the loss associated with shock waves decreases, the resultant strong flow expansion can substantially lower the reactant pressure and lead to a higher performance loss. This phenomenon can be clearly observed from Fig. 17, which shows the time histories of the pressure and reactant mass fraction at the middle of the tube ($x = 25$ cm). For $r_{th}/r_{tube} = 0.6$, the average pressure during the filling process is

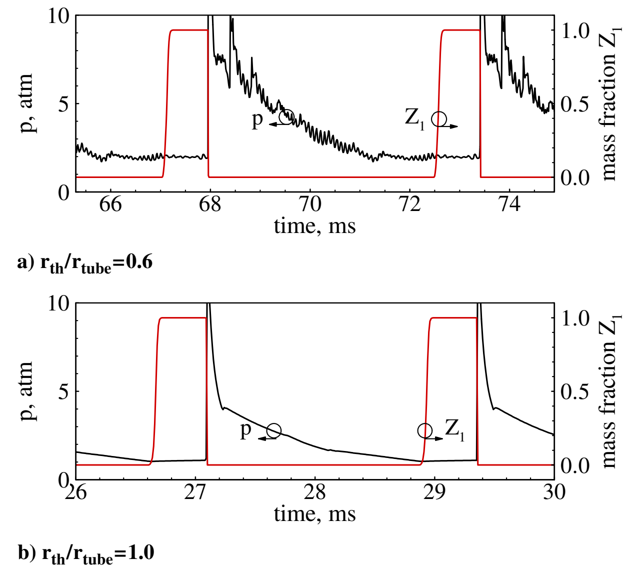

Fig. 17 Time histories of pressure and reactant mass fraction at middle point ($x = 25$ cm) of tube; stoichiometric H_2/air mixture, $h = 9.3$ km, $M_\infty = 2.1$.

2.00 atm, slightly lower than 2.05 atm at the head end, whereas in the straight tube-extension case of $r_{th}/r_{tube} = 1.0$, the average pressure of 1.07 atm is considerably lower than 1.85 atm at the head end. Figure 18 further demonstrates the decrease of the average pressure at the middle of the tube with increasing throat area. On the other hand, as the throat area decreases from its optimum value, the increased nozzle expansion and divergence losses degrade the overall system performance.

Figure 19 shows the influence of the nozzle throat area on the normalized specific impulse and thrust, reaching their optimum values at $r_{th}/r_{tube} = 0.6$ and 0.9, respectively. The thrust increases considerably by about 91% when r_{th}/r_{tube} varies from 0.5 to 0.9, due to the increase in the operating frequency and subsequently the cycle-averaged air mass flow rate. Figure 20 shows the valve operation times as a function of the nozzle throat area. Both the valve-open and valve-closed times decrease with increasing throat area. The cycle period decreases by about 71% as r_{th}/r_{tube} increases from 0.6 to 1.0.

It is worth mentioning that the present work only considers the effect of the nozzle throat area. A complete study on nozzle optimization should include more configuration parameters and should be carried out in the future.

3. *Effect of Flight Conditions*

In addition to the baseline case, several other flight conditions listed in Table 2 are considered to provide a broad assessment of the

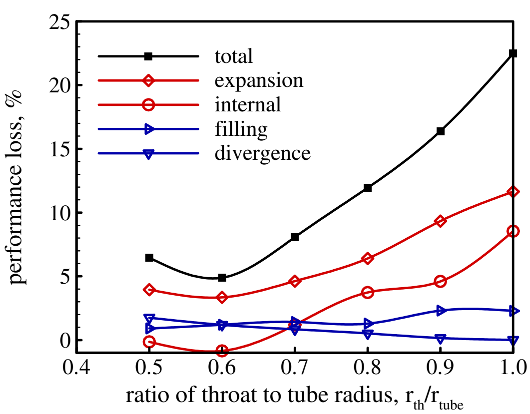

Fig. 16 Effect of nozzle throat area on performance loss; stoichiometric H_2/air mixture, $h = 9.3$ km, $M_\infty = 2.1$.

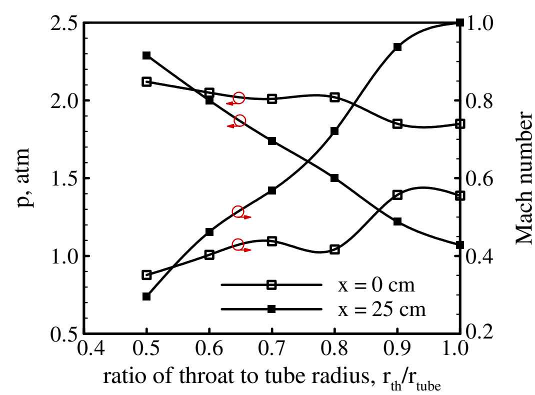

Fig. 18 Time-averaged pressure and Mach number at head end ($x = 0$ cm) and middle point ($x = 25$ cm) of tube during filling process; stoichiometric H_2/air mixture, $h = 9.3$ km, $M_\infty = 2.1$.

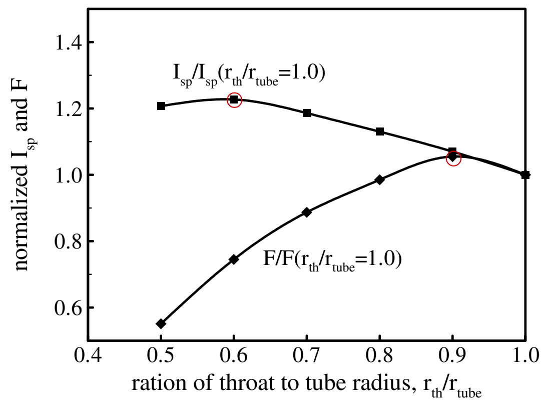

Fig. 19 Normalized specific impulse and thrust as function of nozzle throat area; stoichiometric H_2/air mixture, $h = 9.3$ km, $M_\infty = 2.1$.

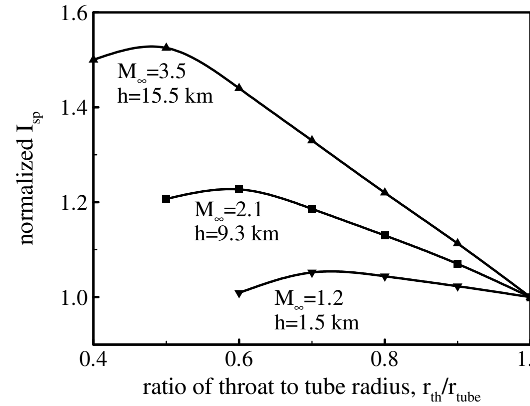

Fig. 21 Effect of nozzle throat on normalized specific impulse I_{sp}/I_{sp} ($r_{th}/r_{tube} = 1.0$); stoichiometric H_2/air mixture. The specific impulses for a straight tube ($r_{th}/r_{tube} = 1.0$) are 3629, 4090, and 3325 s for $M_\infty = 1.2$, 2.1, and 3.5, respectively, and the corresponding maximum I_{sp}'s are 3820, 5020, and 5070 s.

PDE performance. These conditions cover a Mach-number range of 1.2–5.0, with the altitude from 1.5 to 24 km. For the Mach-5 case, the total temperature (1323 K) of the fresh reactants at the combustor entrance well exceeds the autoignition temperature (around 850 K) of the H_2-air mixture. Thus, preignition occurs during the filling stage and causes engine failure. A similar phenomenon was observed in [18]. Figure 21 shows the normalized specific impulse with respect to the value for the straight tube case under various flight conditions as a function of r_{th}/r_{tube}. Similar to the baseline situation, there exists an optimum nozzle throat area for each flight condition. As the Mach number increases, the ratio of the total pressure at the combustor entrance to the ambient pressure increases. A smaller throat is required to preserve the chamber pressure and to match the nozzle exit pressure with the ambient condition more effectively. As a consequence, the relative improvement of the specific impulse with an optimum nozzle throat is more significant at higher flight Mach numbers. These values are 5.2, 23, and 52% for the flight Mach numbers of 1.2, 2.1, and 3.5, respectively.

Figure 22 shows the optimized specific impulse at various flight conditions. Also included for comparison are the theoretical prediction with zero filling Mach number and the ramjet performance. The specific impulse of PDE is higher than its ramjet counterpart by 36, 23, and 3.4% at the flight Mach numbers of 1.2, 2.1, and 3.5, respectively. As a comparison, Harris et al. [18] recently reported a performance gain of 17–26% over ramjet engines for the baseline flight condition with $M_\infty = 2.1$ and $h = 9.3$ km, depending on the ratio of the purge to valve-open time. The performance trend can be explained as follows. At low flight Mach numbers, ram compression is weak. The precompression of reactants by the leading shock wave in a detonation tube becomes important and considerably benefits the engine performance. At high Mach numbers, ram compression is already so strong that the relative benefit of the shock precompression in the chamber becomes weak. At even higher Mach numbers, the performance of a PDE may become lower than its ramjet counterpart due to such intrinsic performance losses associated with the filling, nozzle expansion, and internal-flow processes. Another issue with high flight Mach numbers lies in the fact that the total temperature of reactants may exceed the autoignition point. The resultant preignition severely limits the engine operation regime. In the present study of hydrogen-air mixtures, autoignition takes place at a flight Mach number slightly larger than 3.5. The inclusion of the theoretical prediction for the Mach-5 condition in Fig. 22 is only for the purpose of comparison with ramjet engines.

VII. Summary

The propulsive performance of airbreathing PDEs has been theoretically and numerically studied over a wide range of system configurations, operating parameters, and flight conditions. The work treats detailed detonation propagation and unsteady gasdynamics in the chamber, as well as flow expansion through the nozzle to the ambient. Two different modes of valve operation were considered. The effects of valve operation timing based on different criteria were examined systematically. The influence of nozzle configuration on engine propulsive performance was also investigated. In addition, an analytical model was established to predict the PDE performance with an idealized operation. Results were employed to help identify and quantify the various performance loss mechanisms that degrade the engine propulsive efficiency. A performance map was established over the flight Mach-number range of 1.2–3.5. The PDE outperforms its ramjet counterpart for all the flight conditions considered herein, but the net benefit decreases with increasing flight Mach number.

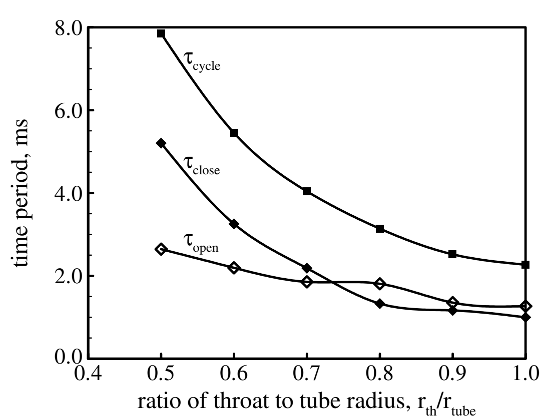

Fig. 20 Effect of nozzle throat area on valve operation times; stoichiometric H_2/air mixture, $h = 9.3$ km, $M_\infty = 2.1$.

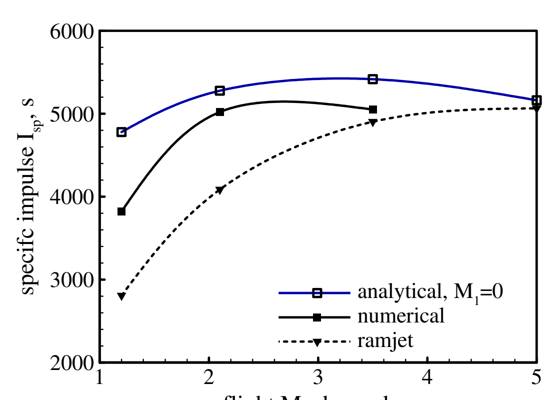

Fig. 22 Specific impulses at various flight conditions; stoichiometric H_2/air mixture.

Acknowledgements

This work was supported by the Department of Defense Multidisciplinary University Research Initiative under the Office of Naval Research Grant N00014-02-1-0589, with Gabriel Roy serving as the Program Manager. The authors are deeply grateful to Paul Harris for extensive discussions on the PDE performance.

References

[1] Kailasanath, K., "Recent Developments in the Research on Pulse Detonation Engines," *AIAA Journal*, Vol. 41, No. 2, 2003, pp. 145–159.

[2] Roy, G. D., Frolov, S. M., Borisov, A. A., and Netzer, D. W., "Pulse Detonation Engine: Challenges, Current Status, and Future Perspective," *Progress in Energy and Combustion Science*, Vol. 30, No. 6, 2004, pp. 545–672.

[3] Ma, F. H., Choi, J. Y., and Yang, V., "Thrust Chamber Dynamics and Propulsive Performance of Single-Tube Pulse Detonation Engines," *Journal of Propulsion and Power*, Vol. 21, No. 3, 2005, pp. 512–526.

[4] Ma, F. H., Choi, J. Y., and Yang, V., "Thrust Chamber Dynamics and Propulsive Performance of Multitube Pulse Detonation Engines," *Journal of Propulsion and Power*, Vol. 21, No. 4, 2005, pp. 681–691.

[5] Wintenberger, E., Austin, J. M., Cooper, M., Jackson, S., and Shepherd, J. E., "An Analytical Model for the Impulse of a Single-Cycle Pulse Detonation Engine," *Journal of Propulsion and Power*, Vol. 19, No. 1, 2003, pp. 22–38.

[6] Hinkey, J. B., Bussing, T. R. A., and Kaye, L., "Shock Tube Experiments for the Development of a Hydrogen-Fueled Pulse Detonation Engine," AIAA Paper 1995-2578, July 1995.

[7] Endo, T., Kasahara, J., Matsuo, A., Inaba, K., Sato, S., and Fujiwara, T., "Pressure History at the Thrust Wall of a Simplified Pulse Detonation Engine," *AIAA Journal*, Vol. 42, No. 9, 2004, pp. 1921–1930.

[8] Kailasanath, K., Patnaik, G., and Li, C., "Computational Studies of Pulse Detonation Engines: A Status Report," AIAA Paper 1999-2634, June 1999.

[9] Radulescu, M. I., and Hanson, R. K., "Effect of Heat Loss on Pulse Detonation Engine Flow Fields and Performance," *Journal of Propulsion and Power*, Vol. 21, No. 2, 2005, pp. 274–285.

[10] Yungster, S., "Analysis of Nozzle Effects on Pulse Detonation Engine Performance," AIAA Paper 2003-1316, Jan. 2003.

[11] Tangirala, V. E., Varatharajan, B., and Dean, A. J., "Numerical Investigations of Detonation Initiation," AIAA Paper 2003-0716, Jan. 2003.

[12] Perkins, H. D., and Sung, C. J., "Effects of Fuel Distribution on Detonation Tube Performance," *Journal of Propulsion and Power*, Vol. 21, No. 3, 2005, pp. 539–545.

[13] Aarnio, M. J., Hinkey, J. B., and Bussing, T. R. A., "Multiple Cycle Detonation Experiments During the Development of a Pulse Detonation Engine," AIAA Paper 1996-3263, July 1996.

[14] Schauer, F., Stutrud, J., and Bradley, R., "Detonation Initiation Studies and Performance Results for Pulsed Detonation Engine Applications," AIAA Paper 2001-1129, Jan. 2001.

[15] Cambier, J. L., and Adelman, H. G., "Preliminary Numerical Simulations of a Pulsed Detonation Wave Engine," AIAA Paper 1988-2960, July 1988.

[16] Cambier, J. L., and Tegner, J. K., "Strategies for Pulsed Detonation Engine Performance Optimization," *Journal of Propulsion and Power*, Vol. 14, No. 4, 1998, pp. 489–498.

[17] Wu, Y. H., Ma, F. H., and Yang, V., "System Performance and Thermodynamic Cycle Analysis of Airbreathing Pulse Detonation Engines," *Journal of Propulsion and Power*, Vol. 19, No. 4, 2003, pp. 556–567.

[18] Harris, P. G., Stowe, R. A., Ripley, R. C., and Guzik, S. M., "Pulse Detonation Engine as a Ramjet Replacement," *Journal of Propulsion and Power*, Vol. 22, No. 2, 2006, pp. 462–473.

[19] Fong, K. K., and Nalim, M. R., "Gas Dynamics Limits and Optimization of Pulsed Detonation Static Thrust," AIAA Paper 2000-3471, July 2000.

[20] Heiser, W. H., and Pratt, D. T., "Thermodynamic Cycle Analysis of Pulse Detonation Engines," *Journal of Propulsion and Power*, Vol. 18, No. 1, 2002, pp. 68–76.

[21] Talley, D. G., and Coy, E. B., "Constant Volume Limit of Pulsed Propulsion for a Constant γ Ideal Gas," *Journal of Propulsion and Power*, Vol. 18, No. 2, 2002, pp. 400–406.

[22] Cooper, M., Jackson, S., Austin, J., Wintenberger, E., and Shepherd, J. E., "Direct Experimental Impulse Measurements for Detonation and Deflagrations," *Journal of Propulsion and Power*, Vol. 18, No. 5, 2002, pp. 1033–1041.

[23] Shehadeh, R., Saretto, S., Lee, S. Y., Pal, S., and Santoro, R. J., "Experimental Study of a Pulse Detonation Engine Ejector," AIAA Paper 2003-4972, July 2003.

[24] Tangirala, V. E., Murrow, K., Fakunle, O., and Dean, A. J., "Thermodynamic and Unsteady Flow Considerations in Performance Estimation for Pulse Detonation Applications," AIAA Paper 2005-0226, Jan. 2005.

[25] Brophy, C. M., Werner, L. S., and Sinibaldi, J. O., "Performance Characterization of a Valveless Pulse Detonation Engine," AIAA Paper 2003-1344, Jan. 2003.

[26] Ma, F. H., and Yang, V., "A Unified Flow Analysis of Valveless Airbreathing Pulse Detonation Engine," *Pulse and Continuous Detonation Propulsion*, edited by G. Roy, and S. Frolov, Torus Press, Moscow, 2006, pp. 219–234.

[27] Oh, J. Y., Ma, F. H., Hsieh, S. Y., and Yang, V., "Interactions Between Shock and Acoustic Waves in a Supersonic Inlet Diffuser," *Journal of Propulsion and Power*, Vol. 21, No. 3, 2005, pp. 486–495.

[28] Mattingly, J. D., Heiser, W. H., and Daley, D. H., *Aircraft Engine Design*, AIAA Education Series, AIAA, New York, 1987.

[29] Choi, J. Y., Kim, D. W., Jeung, I. S., Ma, F. H., and Yang, V., "Cell-Like Structure of Unstable Oblique Detonation Wave from High-Resolution Numerical Simulation," *Proceedings of the Combustion Institute*, Vol. 31, 2006 (to be published).

[30] Mohanraj, R., and Merkle, C. L., "A Numerical Study of Pulse Detonation Engine Performance," AIAA Paper 2000-0315, Jan. 2000.

[31] McBride, B. J., and Gordon, S., "Computer Program for Calculation of Complex Chemical Equilibrium Compositions and Applications," NASA Reference Publ. 1311, June 1996.

[32] Choi, J. Y., Ma, F. H., and Yang, V., "Numerical Simulation of Cellular Structure of Two-Dimensional Detonation Waves," AIAA Paper 2005-1174, Jan. 2005.

[33] Wang, X. Y., and Chang, S. C., "A 2D Non-Splitting Unstructured Triangular Mesh Euler Solver Based on the Space-Time Conservation Element and Solution Element Method," *Computational Fluid Dynamic Journal*, Vol. 8, No. 2, 1999, pp. 309–325.

[34] Wu, Y. H., Ma, F. H., and Yang, V., "Space-Time Method for Detonation Problems with Finite-Rate Chemical Kinetics," *International Journal of Computational Fluid Dynamics*, Vol. 18, No. 3, 2004, pp. 277–287.

[35] Karypis, G., and Kumar, V., "Multilevel K-Way Partitioning Scheme for Irregular Graphs," *Journal of Parallel and Distributed Computing*, Vol. 48, No. 1, 1998, pp. 96–129.

[36] Nicholls, J. A., Wilkinson, H. R., and Morrison, R. B., "Intermittent Detonation as a Thrust-Producing Mechanism," *Jet Propulsion*, Vol. 27, No. 5, 1957, pp. 534–541.

[37] Ma, F. H., "Thrust Chamber Dynamics and Propulsive Performance of Airbreathing Pulse Detonation Engines," Ph.D. Dissertation, Department of Mechanical Engineering, The Pennsylvania State University, University Park, PA, Dec. 2003.

[38] Hodge, B. K., and Koenig, K., *Compressible Fluid Dynamics with Personal Computer Applications*, Prentice–Hall, Englewood Cliffs, NJ, 1995.

[39] Cooper, M., and Shepherd, J. E., "The Effect of Nozzles and Extensions on Detonation Tube Performance," AIAA Paper 2002-3628, July 2002.

[40] Li, C., and Kailasanath, K., "Partial Fuel Filling in Pulse Detonation Engines," *Journal of Propulsion and Power*, Vol. 19, No. 5, 2003, pp. 908–916.

J. Powers
Associate Editor